The Journal of Chemical Physics

The Aharonov-Anandan phase and geometric double-quantum excitation in strongly-coupled nuclear spin pairs

Cite as: J. Chem. Phys. (in press) (2022); https://doi.org/10.1063/5.0138146
Submitted: 08 December 2022 • Accepted: 05 March 2023 • Accepted Manuscript Online: 06 March 2023

Christian Bengs, Mohamed Sabba and Malcolm H. Levitt

AIP Publishing

Accepted to J. Chem. Phys. 10.1063/5.0138146

The Aharonov-Anandan phase and geometric double-quantum excitation in strongly-coupled nuclear spin pairs

Christian Bengs,[a] Mohamed Sabba,[b] and Malcolm H. Levitt[c]
School of Chemistry, University of Southampton, SO17 1BJ, UK

(Dated: February 1, 2023)

The Aharonov-Anandan phase is a contribution to the phase acquired by cyclic evolution of a quantum state which depends only on the geometric properties of its trajectory. We report the study and the exploitation of the Aharonov-Anandan phase by NMR interferometry techniques in homonuclear spin-1/2 pairs in the near-equivalence limit. We introduce a new method for engineering effective zero-quantum Hamiltonians with arbitrary phase in the transverse plane. We use this method to generate a variety of cyclic zero-quantum paths enabling direct study of the geometric Aharonov-Anandan phase to probe the rotational characteristics of the zero-quantum subspace. We show that the geometric Aharonov-Anandan phase may be used for efficient double-quantum excitation in strongly coupled spin pairs. We find that geometric double-quantum excitation outperforms the standard method by a factor of two in experiments performed on a typical case involving near-equivalent spin pairs.

I. INTRODUCTION

Cyclic evolution of a physical system is typically considered to be any process that eventually leads to the return of the systems state to its original value. Although this intuitive definition might be true in most classical situations, quantum systems undergoing cyclic evolution do in general not follow this rule. Instead, the initial and final state of the quantum system may differ by a meaningful phase factor. This particularly intriguing quantum phenomenon has first been described by Berry[1] in the context of adiabatic cyclic quantum evolution. Berry has shown that the final phase of the quantum state is a well-defined combination of a dynamic phase and a geometric phase. The geometric phase only depends on the geometry of the parameter curve of the adiabatic Hamiltonian, but not on the detailed dynamics along the curve. This concept was later generalised by Aharonov and Anandan[2], lifting the adiabaticity condition, and rephrasing the argument in terms of the cyclic evolution of pure state density operators rather than parameter space trajectories.

Since then experimental demonstrations of the geometric phase have been performed by NMR interferometry[3,4]. However, so far such demonstrations have only been performed on isolated or weakly-coupled spin systems[5–11], and without much emphasis on any practical applications of such phenomena. Here we describe theoretically, and demonstrate experimentally, the direct measurement of geometric phase factors in coupled pairs of ^{13}C nuclei in the near-equivalence regime. This is an important regime for NMR experiments involving long-lived spin states such as nuclear singlet order[12–19].

Strongly-coupled spin pairs are difficult to manipulate in the near-equivalence limit. The vanishing resonance frequency difference between the spins complicates the application of local rotations as the spins respond identically to the application of external magnetic fields. We address this issue by introducing a new technique to engineer arbitrary effective Hamiltonians in the zero-quantum subspace. This method is used to construct a set of cyclic trajectories in the zero-quantum subspace. In each case, evolution of the spin system through the cyclic trajectory generates a geometric, or Aharonov-Anandan, phase, defined by the geometric properties of the trajectory, and which is measured by NMR interferometry. These experiments also reveal the spinor character of the zero-quantum subspace of a strongly-coupled spin-1/2 pair.

We further demonstrate that the geometric phase may be exploited for efficient double-quantum excitation in nearly-equivalent spin-1/2 pairs. Double-quantum NMR methods have been used extensively for spectral editing[20], and for ^{13}C spectral assignment[21]. In addition, the relaxation of double-quantum coherences is sensitive to cross-correlation effects, thereby providing information on molecular geometry[22–24].

However, most double-quantum excitation schemes are tailored towards weakly-coupled spin systems. One such example is the INADEQUATE[20,25] experiment (incredible natural abundance double quantum transfer experiment), which was originally developed for the selection of satellite signals in natural abundance ^{13}C compounds. The INADEQUATE sequence is also capable of exciting double-quantum coherences in strongly coupled spin systems as discussed by Nakai and McDowell[26]. However, in the near-equivalence limit, the double-quantum excitation time scales as $T_{\mathrm{DQ}} \sim J/(\Delta^2)$, where Δ represents the resonance frequency difference, and J the scalar coupling constant between the two spins[27]. The long double-quantum excitation time leads to considerable relaxation losses.

As discussed below, the long double-quantum excitation times may be attributed to an exclusive re-

[a] cb1d19@soton.ac.uk
[b] m.sabba@soton.ac.uk
[c] mhl@soton.ac.uk

liance on the dynamic phases acquired by the quantum states. As shown below, it is possible to design more efficient double-quantum excitation schemes in the near-equivalence regime with double-quantum excitation times on the order of $T_{\mathrm{DQ}} \sim \pi/(2\Delta)$, by exploiting the geometric Aharonov-Anandan phase. We call this approach *geometric double-quantum excitation.*

II. THE AHARONOV-ANANDAN PHASE

Consider the evolution of a pure quantum state $|\psi(t)\rangle$ returning to its initial value $|\psi(0)\rangle$ at time $t = T$ up to some phase factor ϕ_{tot}

$$|\psi(T)\rangle = \exp(+i\phi_{\mathrm{tot}})|\psi(0)\rangle. \tag{1}$$

The evolution of $|\psi(t)\rangle$ induces a closed curve $\mathcal{C}$ (in example a periodic, non-constant curve[28]) in the projective Hilbert space $\mathcal{P}(\mathcal{H})$.

$$|\psi(T)\rangle\langle\psi(T)| = |\psi(0)\rangle\langle\psi(0)|. \tag{2}$$

The evolution time T may be regarded as the period of the cycle $\mathcal{C}$ in $\mathcal{P}(\mathcal{H})$.

Aharonov and Anandan[2] have shown that the accumulated phase ϕ_{tot} acquired over the cycle $\mathcal{C}$ may be split into a dynamic phase factor ϕ_{dyn} and a geometric phase factor ϕ_{geo}

$$\phi_{\mathrm{tot}} = \phi_{\mathrm{dyn}} + \phi_{\mathrm{geo}}. \tag{3}$$

The dynamic phase encodes information about the Hamiltonian of the system and may be calculated as follows

$$\phi_{\mathrm{dyn}} = -i \int_0^T \langle\psi(t)|\frac{d}{dt}\psi(t)\rangle dt. \tag{4}$$

The geometric phase ϕ_{geo} does not depend upon the exact dynamics of the system but only on the geometric properties of the curve traced out in $\mathcal{P}(\mathcal{H})$. In the case of a two-level system, for example, $\mathcal{P}(\mathcal{H})$ may be identified with the Bloch sphere. For a closed curve on S^2 the geometric phase is given up to a sign by one-half of the solid angle subtended by the cycle $\mathcal{C}$ at the origin of the unit sphere (see supplement)

$$\phi_{\mathrm{geo}}(\mathcal{C}) = \pm\tfrac{1}{2}\boldsymbol{\Omega}(\mathcal{C}), \tag{5}$$

The sign depends in general on the details of the cyclic evolution, for example the sense in which the cycle is traversed.

In the case of adiabatic cyclic transformations of spin states, for example by a slow variation in the direction of a magnetic field, the geometric or Aharonov-Anandan phase is identical to Berry's phase[1,2]. However, the Aharonov-Anandan phase is more general than Berry's phase, since adiabaticity is not required. The experiments described in this paper do not involve adiabatic transformations, and exploit the Aharonov-Anandan phase, not Berry's phase.

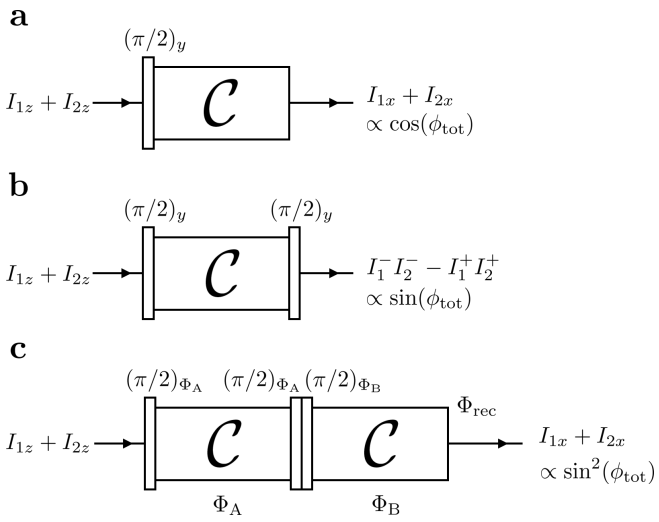

Figure 1. General pulse sequences for NMR interferometry and double-quantum experiments on near-equivalent spin pairs. (a) NMR interferometry. The initial z-magnetisation is converted into single-quantum triplet-triplet spin coherences. A zero-quantum cycle $\mathcal{C}$ (equation 2) gives the pair of triplet-triplet coherences a phase difference ϕ_{tot} given by the sum of the dynamic phase ϕ_{dyn} and the geometric phase ϕ_{geo} (equation 3) for the cycle. Interference between the coherences leads to an amplitude modulation of the transverse magnetisation. The signal amplitude is proportional to $\cos(\phi_{\mathrm{tot}})$. (b) Double-quantum excitation. The additional $(\pi/2)_y$ pulse excites double quantum coherences with an amplitude proportional to $\sin(\phi_{\mathrm{tot}})$. (c) Double-quantum filtration. The first pulse sequence block excites double-quantum terms in the density operator with the phases of all pulse elements being shifted by Φ_{A}. For the reconversion step all pulse sequence elements are shifted by Φ_{B} with the final $\pi/2$ pulse omitted. This has the effect of converting double-quantum terms into observable magnetisation. Lastly, the phase of the receiver is set to Φ_{rec}. Double-quantum filtration is achieved by averaging over individual transients in combination with a suitable choice of the phases Φ_{A}, Φ_{B}, Φ_{rec} a typical example being the four-step phase cycle given by $\Phi_{\mathrm{A}} = \{0, 0, 0, 0\}$, $\Phi_{\mathrm{B}} = \{0, \frac{1}{2}\pi, \pi, \frac{3}{2}\pi\}$ and $\Phi_{\mathrm{rec}} = \{0, \frac{3}{2}\pi, \pi, \frac{1}{2}\pi\}$[29,30].

III. MANIPULATIONS OF STRONGLY COUPLED SPIN-1/2 PAIRS

A. NMR interferometry

The Aharonov-Anandan phase may be studied by NMR interferometry[3,4,6]. Consider for example the pulse sequence shown in figure 1a. The pulse sequence consists of an initial $(\pi/2)_y$ pulse followed by a cyclic pulse sequence element $\mathcal{C}$, and a detection period. This works as follows: Initially the spins are at thermal equilibrium (figure 2a). The density operator for a thermally equilibrated ensemble of near-equivalent spin-1/2 pairs in the

Accepted to J. Chem. Phys. 10.1063/5.0138146

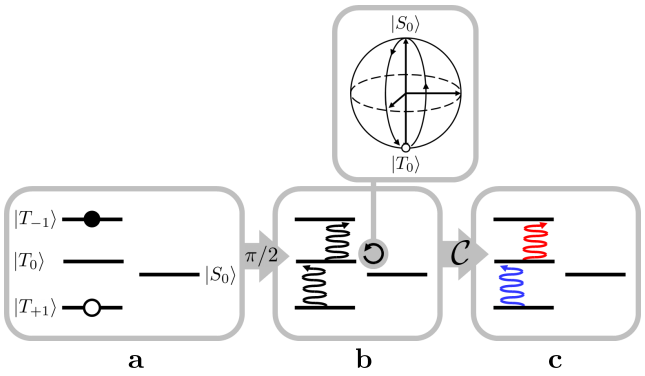

Figure 2. Spin-state evolution under the NMR interferometry experiment shown in figure 1. (a) Excess populations of the spin system in thermal equilibrium. (b) Single-quantum triplet-triplet coherences excited by the initial $(\pi/2)$ pulse are indicated by a curvy arrow. Cyclic evolution in the $|T_0\rangle$-$|S_0\rangle$ subspace (see inset) imposes a phase factor on the $|T_0\rangle$ state. (c) The opposite phase factors for the two (-1)-quantum coherences are indicated by colours. This phase difference is observable as a modulation of the spectral intensity.

high temperature limit is given approximately by[29]

$$\begin{aligned}\rho_{\mathrm{eq}} &\simeq \tfrac{1}{4}\mathbb{1} + M_{\mathrm{eq}}(I_{1z} + I_{2z}) \\ &= \tfrac{1}{4}\mathbb{1} + M_{\mathrm{eq}}(|T_{+1}\rangle\langle T_{+1}| - |T_{-1}\rangle\langle T_{-1}|),\end{aligned} \tag{6}$$

where the nuclear singlet and triplet states, and their numbering, are given by

$$\begin{array}{rcll} |1\rangle &=& |S_0\rangle &= (|\alpha\beta\rangle - |\beta\alpha\rangle)/\sqrt{2}, \\ |2\rangle &=& |T_{+1}\rangle &= |\alpha\alpha\rangle\,, \\ |3\rangle &=& |T_0\rangle &= (|\alpha\beta\rangle + |\beta\alpha\rangle)/\sqrt{2}, \\ |4\rangle &=& |T_{-1}\rangle &= |\beta\beta\rangle\,, \end{array} \tag{7}$$

and M_{eq} represents the equilibrium magnetization of the spin ensemble.

An initial $(\pi/2)_y$-pulse generates a pair of coherences between the outer triplet states and the central triplet state (see figure 2b)

$$\begin{aligned}\rho(0) &= \tfrac{1}{4}\mathbb{1} + M_{\mathrm{eq}}(I_{1x} + I_{2x}) \\ &= \tfrac{1}{4}\mathbb{1} + M_{\mathrm{eq}}\{|T_0\rangle(\langle T_{+1}| + \langle T_{-1}|) + \mathrm{h.c.}\},\end{aligned} \tag{8}$$

where h.c. refers to the hermitian conjugate. Suppose now that we are able to generate a unitary operation $V(T)$ of the type

$$\begin{aligned} &V(T)|S_0\rangle = \exp(+i\xi)|S_0\rangle, \\ &V(T)|T_0\rangle = \exp(+i\phi_{\mathrm{tot}})|T_0\rangle, \\ &V(T)(|T_{+1}\rangle + |T_{-1}\rangle) = |T_{+1}\rangle + |T_{-1}\rangle. \end{aligned} \tag{9}$$

The unitary operation $V(T)$ has no net effect on the outer triplet states but imposes phase factors on the central triplet state and the singlet state. As indicated in figure 2c the operation $V(T)$ generates a cyclic evolution within the $\{|S_0\rangle, |T_0\rangle\}$ subspace, leading in general to a phase change in the observable single-quantum coherence. Focusing on the traceless part of the density operator, the action of $V(T)$ may be expressed as follows

$$\begin{aligned}\rho(T) &= V(T)(I_{1x} + I_{2x})V^{\dagger}(T) \\ &= 2^{-1/2}\exp(+i\phi_{\mathrm{tot}})|T_0\rangle(\langle T_{+1}| + \langle T_{-1}|) + \mathrm{h.c.} \\ &= \cos(\phi_{\mathrm{tot}})(I_{1x} + I_{2x}) + 2\sin(\phi_{\mathrm{tot}})(I_{1y}I_{2z} + I_{1z}I_{2y}),\end{aligned} \tag{10}$$

and the total phase acquired by the $|T_0\rangle$ state is encoded as an amplitude modulation of the transverse magnetization. This is in contrast to the original interferometry experiments performed by Suter *et al.*[4] where the acquired phase is encoded as a phase shift of the transverse magnetization. The modulation of the triplet signal amplitude by a rotation in the zero-quantum subspace was previously demonstrated in the context of singlet NMR by Tayler and Levitt[31]. In that case, the effect was exploited to optimize the pulse sequence parameters for the generation of nuclear singlet order.

The phase of the $|T_0\rangle$ state may therefore be inferred from the observed signal intensity of the NMR spectrum $S(\omega)$. Since the intensity of the imaginary part of the spectrum is given by the first "point" of the NMR signal $s(t)$ we simply have

$$\langle S(\omega)\rangle = \int_{-\infty}^{+\infty} \mathrm{Im}\{S(\omega)\}d\omega = \mathrm{Im}\{s(0)\} = \cos(\phi_{\mathrm{tot}}). \tag{11}$$

The total phase ϕ_{tot} is the sum of the dynamic phase ϕ_{dyn} and the geometric phase ϕ_{geo} (equation 3). Hence, the geometric phase ϕ_{geo} may be estimated for any cyclic trajectory in the $\{|S_0\rangle, |T_0\rangle\}$ subspace, providing that the dynamic phase contribution ϕ_{dyn} is known. In some cases, the dynamic phase ϕ_{dyn} vanishes, so that the signal amplitude only depends on the geometric phase ϕ_{geo}. Some specific cases are discussed in detail below.

B. Geometric Double-Quantum Excitation

The NMR interferometry experiment may be extended to achieve double-quantum excitation in strongly coupled spin-1/2 pairs, by appending a $(\pi/2)_y$ pulse, as shown in figure 1b. To see how double-quantum excitation occurs consider the last term in equation 10. Application of a $\pi/2$ pulse along the rotating frame y-axis transforms these spin operators into double-quantum coherence operators:

$$\begin{aligned}2R_y(\pi/2)(I_{1y}I_{2z} + I_{1z}I_{2y})R_y^{\dagger}(\pi/2) &= 2(I_{1y}I_{2x} + I_{1z}I_{2x}) \\ &= i(I_1^-I_2^- - I_1^+I_2^+).\end{aligned} \tag{12}$$

The observed double-quantum amplitude a_{DQ} is thus directly related to the total phase ϕ_{tot} as follows

$$a_{\mathrm{DQ}} = \sin(\phi_{\mathrm{tot}}). \tag{13}$$

This observation indicates that the cycle $\mathcal{C}$ should be chosen to generate a total phase of $\phi_{\mathrm{tot}} = \pi/2$ in order to

provide double-quantum excitation in nearly-equivalent spin pairs.

In conventional double-quantum excitation schemes on weakly-coupled spin systems, such as the INADEQUATE pulse sequence, the total phase $\phi_{\mathrm{tot}} \simeq \pi/2$ is dominated by the dynamic phase ϕ_{dyn}, with the geometric phase ϕ_{geo} playing a negligible role. However, this approach becomes ineffective in the case of near-equivalent spin-1/2 pairs, since very long evolution intervals are required to build up a sufficient dynamic phase angle[26,27]. Fortunately, as shown below, the geometric phase ϕ_{geo} may be exploited in this regime, leading to efficient double-quantum excitation even when the chemical shift difference is much smaller than the J-coupling. We call this approach *geometric double-quantum excitation.*

C. Double-Quantum Filtration

Geometric double-quantum excitation blocks may be incorporated into double-quantum filtration schemes as shown in figure 1c. The basic filtration scheme consists of double-quantum excitation blocks in combination with a suitable phase cycle. The first block has all its pulses shifted by an overall Φ_{A}, and is responsible for double-quantum excitation. The second block has all its phases shifted by Φ_{B}, and is responsible for reconversion of double-quantum terms into observable magnetisation, which explains the absence of the final 90°. The receiver phase Φ_{rec} represents an additional degree of freedom. For the current case double-quantum filtration occurs between the two excitation blocks.

Consider now the application of the double-quantum excitation block with all phases shifted by Φ_{A}. Utilising equation 10 the resulting density operator ρ_{A} takes the form

$$\rho_{\mathrm{A}} = i\sin(\phi_{\mathrm{tot}})\{e^{-2i\Phi_{\mathrm{A}}} I_1^- I_2^- - e^{+2i\Phi_{\mathrm{A}}} I_1^+ I_2^+\} + \ldots \tag{14}$$

Application of a second double-quantum excitation block phase-shifted by Φ_{B} and missing its final 90° pulse leads to

$$\rho_{\mathrm{B}} = \frac{i}{4}\sin^2(\phi_{\mathrm{tot}}) e^{-i(2\Phi_{\mathrm{A}}+\Phi_{\mathrm{B}})}(e^{i4\Phi_{\mathrm{A}}} + e^{i4\Phi_{\mathrm{B}}})(I_1^- + I_2^-) + \ldots. \tag{15}$$

Taking the receiver phase into account the resulting signal amplitude may be expressed as follows

$$a(\Phi) = \frac{i}{4}\sin^2(\phi_{\mathrm{tot}}) e^{-i(2\Phi_{\mathrm{A}}+\Phi_{\mathrm{B}}+\Phi_{\mathrm{rec}})}(e^{i4\Phi_{\mathrm{A}}} + e^{i4\Phi_{\mathrm{B}}}). \tag{16}$$

For a four-step double-quantum phase cycle (an example is given in the caption of figure 1) the *double-quantum filtered* signal amplitude reduces to

$$a_{\mathrm{DQF}} = 2i\sin^2(\phi_{\mathrm{tot}}), \tag{17}$$

and is thus proportional to $\sin^2(\phi_{\mathrm{tot}})$. Any signals deriving from undesirable coherences generated by the double-quantum excitation step are suppressed by the phase cycle.

IV. ZERO-QUANTUM HAMILTONIAN ENGINEERING

We now consider the construction of the unitary operation $V(T)$ given by equation 9. The rotating-frame Hamiltonian for a strongly coupled spin-1/2 pair in solution may be expressed as follows[29]

$$\begin{aligned} H_0 &= \frac{1}{2}\omega_\Delta(I_{1z} - I_{2z}) + \omega_J \mathbf{I}_1 \cdot \mathbf{I}_2, \\ \omega_\Delta &= \omega_1^0 - \omega_2^0 = 2\pi\Delta, \\ \omega_J &= 2\pi J, \end{aligned} \tag{18}$$

where we assumed the reference frequency to be centred between the resonance frequencies of the two spins. The (rotating-frame) resonance frequency difference of the spins is given by ω_Δ, while ω_J represents the mutual scalar coupling.

We may express the Hamiltonian of the system as follows

$$H_0 = \Omega\left(\frac{1}{2}\sin(\theta_{\mathrm{ST}})(I_{1z} - I_{2z}) + \cos(\theta_{\mathrm{ST}})(\mathbf{I}_1 \cdot \mathbf{I}_2)\right), \tag{19}$$

where Ω represents the effective frequency of the system

$$\Omega = 2\pi\sqrt{J^2 + \Delta^2} \tag{20}$$

and the angle θ_{ST} quantifies the mixing of the central triplet state and the singlet state

$$\theta_{\mathrm{ST}} = \arctan(\frac{\Delta}{J}). \tag{21}$$

The mixing angle measures how much the singlet and triplet states deviate from the true eigenstates of the Hamiltonian H_0

$$\begin{aligned} |S_0\rangle' &= \cos(\tfrac{1}{2}\theta_{\mathrm{ST}})|S_0\rangle + \sin(\tfrac{1}{2}\theta_{\mathrm{ST}})|T_0\rangle, \\ |T_0\rangle' &= \sin(\tfrac{1}{2}\theta_{\mathrm{ST}})|S_0\rangle - \cos(\tfrac{1}{2}\theta_{\mathrm{ST}})|T_0\rangle. \end{aligned} \tag{22}$$

For convenience we introduce the energy shift operator ΔE

$$\Delta E = -\frac{1}{4}\Omega\cos(\theta_{\mathrm{ST}})\mathbb{1}, \tag{23}$$

and define the energy-shifted Hamiltonian H_0' as follows

$$H_0' = H_0 + \Delta E. \tag{24}$$

The dynamics remain unchanged by this transformation, but the Hamiltonian H_0' has the advantage that it does not contain any trivial phase evolution of the triplet

states. By making use of single transition operators I_{μ}^{rs} as described by Wokaun and Ernst [32], and Vega [33].

$$\begin{aligned} I_x^{rs} &= \frac{1}{2}\big(|r\rangle\langle s| + |s\rangle\langle r| \big), \\ I_y^{rs} &= \frac{1}{2i}\big(|r\rangle\langle s| - |s\rangle\langle r| \big), \\ I_z^{rs} &= \frac{1}{2}\big(|r\rangle\langle r| - |s\rangle\langle s| \big), \\ \mathbb{1}^{rs} &= \big(|r\rangle\langle r| + |s\rangle\langle s| \big), \end{aligned} \tag{25}$$

the Hamiltonian $H_0^{'}$ takes the form[13,14,34,35]

$$H_0^{'} = \Omega(\sin(\theta_{\mathrm{ST}})I_x^{13} - \cos(\theta_{\mathrm{ST}})I_z^{13} - \tfrac{1}{2}\cos(\theta_{\mathrm{ST}})\mathbb{1}^{13}), \tag{26}$$

acting only on states 1 and 3, i.e. the singlet state $|S_0\rangle$ and the central triplet state $|T_0\rangle$.

Consider now a *time-shifted spin echo (TSSE)* sequence of duration $\tau_{\mathrm{e}} = 2\tau + \delta\tau$ consisting of two delays bracketing a single π pulse along the rotating frame y-axis:

$$\mathrm{TSSE} = (\tau + \delta\tau) - (\pi_y) - (\tau). \tag{27}$$

Here, $\delta\tau$ represents a temporal shift of the π-pulse from an ideal spin echo and $(\pi)_y$ is a 180° pulse along the rotating frame y-axis. Within the single-transition operator formalism the total spin-echo propagator may be written as[34]

$$\begin{aligned} U_{\mathrm{TSSE}} =& (i\mathbb{1}^{24})R_x^{24}(\pi)\times \\ & (i\mathbb{1}^{13})\exp(-iH_0^{'}\tau)R_z^{13}(\pi)\exp(-iH_0^{'}(\tau+\delta\tau)). \end{aligned} \tag{28}$$

Suppose the interval τ takes one of the two values

$$\tau_{\pm} = \Omega^{-1}\{\pi - \tfrac{1}{2}\Omega\delta\tau \pm \arccos\left(\cos\left(\tfrac{1}{2}\Omega\delta\tau\right)\tan^2\left(\theta_{\mathrm{ST}}\right)\right)\}, \tag{29}$$

and the time shift $\delta\tau$ is constrained to the closed interval

$$\delta\tau \in 2\pi/\Omega \times [\,-1/2, +1/2]. \tag{30}$$

To first order in θ_{ST} the total echo duration is then given by

$$\tau_{\mathrm{e}}^{\pm} = 2\tau_{\pm} + \delta\tau = \pi/\Omega(2 \mp 1) + \mathcal{O}(\theta_{\mathrm{ST}}^2), \tag{31}$$

and the action of the shifted echo propagator may be described by an effective Hamiltonian of the form

$$H_{\mathrm{eff}}(\tau_{\pm}) = \omega_{\pm}^{13} I_{\phi}^{13} - \tfrac{1}{2}\Omega\cos\left(\theta_{\mathrm{ST}}\right)\mathbb{1}^{13} + \mathcal{O}(\theta_{\mathrm{ST}}^2), \tag{32}$$

where I_{ϕ}^{13} represents a spin operator with ϕ in the transverse plane

$$I_{\phi}^{13} = \cos\left(\phi\right)I_x^{13} + \sin\left(\phi\right)I_y^{13}. \tag{33}$$

The angular frequencies $\omega_{\pm}^{13}$ are given by

$$\begin{aligned} \omega_{+}^{13} &= 2\theta_{\mathrm{ST}}/(2\tau_{+} + \delta\tau), \\ \omega_{-}^{13} &= (2\pi - 2\theta_{\mathrm{ST}})/(2\tau_{-} + \delta\tau), \end{aligned} \tag{34}$$

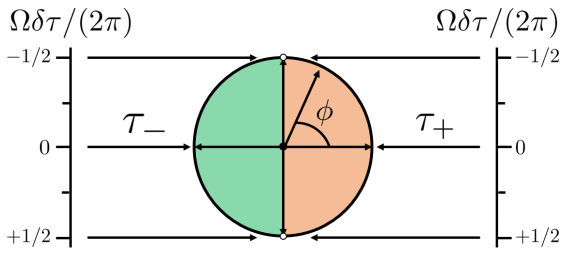

Figure 3. Rotation phase of the effective Hamiltonian of a time-shifted spin echo (equation 27) as a function of the echo shift $\delta\tau$. The τ_+ condition may be used to cover phases in the range $\phi \in [\,-\pi/2, +\pi/2]$, whereas the τ_- condition may be used to cover phases in the range $\phi \in [\,+\pi/2, +3\pi/2]$. A complete covering of the circle requires switching between the two conditions.

whereas the phase ϕ is given by

$$\phi = \frac{1}{2}\Omega\delta\tau. \tag{35}$$

Equation 35 indicates that the phase of the effective Hamiltonian may be manipulated by choosing a suitable echo shift $\delta\tau$

$$\delta\tau = 2\frac{\phi}{\Omega}. \tag{36}$$

where Ω is given by equation 20.

From equation 30 it follows that the phase is restricted to the interval

$$\phi \in [\,-\pi/2, +\pi/2]. \tag{37}$$

Angular frequencies ω_{+}^{13} correspond to anti-clockwise rotations and angular frequencies ω_{-}^{13} correspond to clockwise rotations (ignoring the factor of 2π). By switching between the τ_+ and τ_- condition it is thus possible to generate effective Hamiltonians pointing along *any* axis in the x-y plane of the zero-quantum subspace (see figure 3). Hence the time-shifted echo propagator in the $\{|S_0\rangle, |T_0\rangle\}$ subspace is as follows

$$U_{\pm} = \pm\, i\mathbb{1}^{13}\exp(+i\pi J(2\tau_{\pm} + \delta\tau)\mathbb{1}^{13})R_{\phi}^{13}(\mp 2\theta_{\mathrm{ST}}), \tag{38}$$

where $R_{\phi}^{13}(\theta)$ represents a rotation with phase ϕ through an angle θ in the $\{|S_0\rangle, |T_0\rangle\}$ subspace

$$R_{\phi}^{13}(\theta) = \exp(-i\theta I_{\phi}^{13}). \tag{39}$$

The n-fold repetition of a time-shifted echo takes the simple form

$$U_{\pm}^{n} = (\pm i)^n\mathbb{1}^{13}\exp(+in\pi J(2\tau_{\pm} + \delta\tau)\mathbb{1}^{13})R_{\phi}^{13}(\mp 2n\theta_{\mathrm{ST}}). \tag{40}$$

V. ZERO-QUANTUM CYCLES

Since the $\{|S_0\rangle, |T_0\rangle\}$ subspace comprises a fictitious spin-1/2 system, any pure state may be represented by

Accepted to J. Chem. Phys. 10.1063/5.0138146

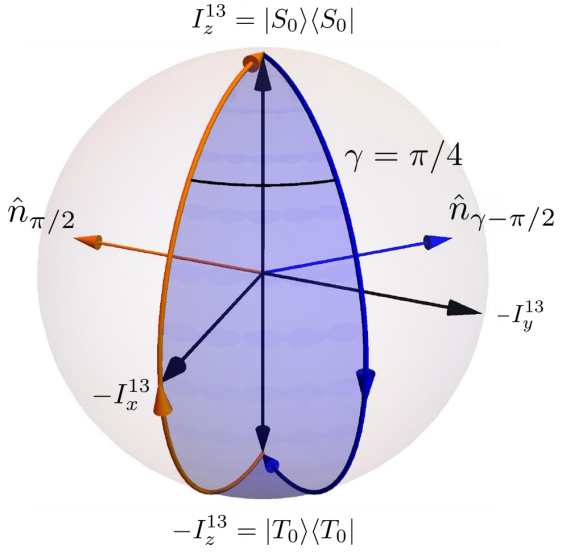

Figure 4. Bloch sphere trajectory in the $\{|S_0\rangle, |T_0\rangle\}$ subspace tracing out the path of a spherical lune with opening angle $\gamma = \pi/4$. The initial $(\pi)_y$ rotation (orange path) transforms the central triplet state into the singlet state. The second (π) rotation (blue path) with phase $\phi = \gamma - \pi/2$ completes the cycle by returning the singlet state to the triplet state.

a point on the Bloch sphere[29]. As a result, trajectories forming a closed curves on the Bloch sphere generate a cycle in the sense of equations 1 and 2. States taken through such trajectories acquire a dynamic phase $\phi_{\rm dyn}$ (equation 4) and a geometric Aharonov-Anandan phase $\phi_{\rm geo}$ (equation 5).

A. Spherical lune

Suppose that the Bloch sphere trajectory of the fictitious spin-1/2 system traces out the path of a *spherical lune* with opening angle γ generated by the following sequence of rotations (see figure 4)

$$V^{\gamma}_{\rm lune}(T) = R^{13}_{\gamma-\pi/2}(\pi) R^{13}_{y}(\pi). \tag{41}$$

The solid angle subtended by a lune of opening angle γ, which is equal to the enclosed surface area on the unit sphere, is given by

$$\mathbf{\Omega}(\mathcal{C}^{\gamma}_{\rm lune}) = 2\gamma. \tag{42}$$

It follows that the geometric phase generated by a trajectory which follows the boundary of the lune is given by

$$\phi_{\rm geo}(\mathcal{C}^{\gamma}_{\rm lune}) = \pm\gamma. \tag{43}$$

where the sign depends on the sense of the traverse. As shown in the SI, the dynamic phase vanishes for the cycle $\mathcal{C}^{\gamma}_{\rm lune}$

$$\phi_{\rm dyn}(\mathcal{C}^{\gamma}_{\rm lune}) = 0. \tag{44}$$

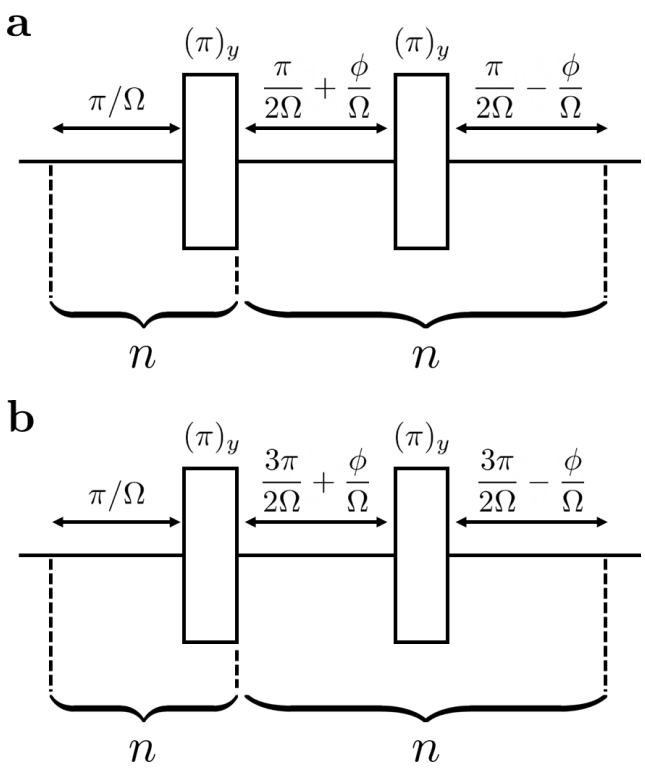

Figure 5. Pulse sequence for generating a spherical lune in the $\{|S_0\rangle, |T_0\rangle\}$ subspace (figure 4). The number of repetitions n of the two parts of the sequence are equal and chosen to satisfy $2n\theta_{\rm ST} = \pi$. The sequence shown in (a) applies for phases within the range $-\pi/2 < \phi < +\pi/2$. The first echo block generates an effective y-rotation in the $\{|S_0\rangle, |T_0\rangle\}$ subspace as described by equation 32. The second echo block generates an effective rotation with phase $\phi = \gamma - \pi/2$ and generates the second half of the spherical lune with opening angle $\gamma = \phi + \pi/2$. The sequence shown in (b) applies for phases within the range $+\pi/2 < \phi < +3\pi/2$. The first echo block generates an effective y-rotation in the $\{|S_0\rangle, |T_0\rangle\}$ subspace, whereas the second echo block generates an effective Hamiltonian with phase $\phi = \gamma - \pi/2$ completing a spherical lune with opening angle $\gamma = \phi + \pi/2$. In each case the entire pulse sequence is deployed as a cycle $\mathcal{C}$ in the schemes of figure 1.

It follows that the total phase is exclusively generated by the geometric (Aharonov-Anandan) phase in this case, and is given by

$$\phi_{\rm tot}(\mathcal{C}^{\gamma}_{\rm lune}) = \pm\gamma. \tag{45}$$

The cycle $\mathcal{C}^{\gamma}_{\rm lune}$ may be implemented by a series of repeated time-shifted echo blocks as shown in figure 5. The first set of time-shifted echoes generates a y-rotation in the $\{|S_0\rangle, |T_0\rangle\}$ subspace. Since each echo induces a rotation through an angle $2\theta_{\rm ST}$, the echo number is chosen to approximately satisfy

$$2n\theta_{\rm ST} \simeq \pi, \tag{46}$$

leading to an overall π rotation. The second set of time-shifted echoes utilises the same number of echoes, but the

Accepted to J. Chem. Phys. 10.1063/5.0138146

position of the rf-pulse is varied to generate an effective Hamiltonian with phase ϕ. As may be seen from figure 5 the phase of the Hamiltonian is related to the opening angle of the lune as follows

$$\phi = \gamma - \pi/2. \tag{47}$$

Additionally, the sequence has no net effect on the state $|T_{+1}\rangle + |T_{-1}\rangle$ thus satisfying the conditions of equation 9 (see supplement). As a result equation 11 in combination with equation 45 indicate that the geometric phase may be directly inferred from the observed spectral intensity in an NMR interferometry experiment:

$$\langle S^{\gamma}_{\text{lune}}(\omega)\rangle \propto \cos(\tfrac{1}{2}\boldsymbol{\Omega}(\mathcal{C}^{\gamma}_{\text{lune}})). \tag{48}$$

A full recovery of the spectral intensity is observed after application of a cycle $\mathcal{C}^{\gamma}_{\text{lune}}$ with a solid angle of 4π. The spherical lune experiment therefore highlights the characteristic 4π-spinor property of the fictitious $\{|S_0\rangle, |T_0\rangle\}$ two-level system. This may also be seen by applying some simple rotation algebra to equation 41

$$\begin{aligned} V^{\gamma}_{\text{lune}}(T) &= R^{13}_{\gamma-\pi/2}(\pi)R^{13}_{y}(\pi) \\ &= R^{13}_{z}(\gamma-\pi/2)R^{13}_{x}(\pi)R^{13}_{z}(-\gamma+\pi/2)R^{13}_{y}(\pi) \\ &= R^{13}_{z}(2\gamma-\pi)R^{13}_{x}(\pi)R^{13}_{y}(\pi) \\ &= R^{13}_{z}(2\gamma-\pi)R^{13}_{z}(\pi) \\ &= R^{13}_{z}(2\gamma) \\ &= R^{13}_{z}(\boldsymbol{\Omega}(\mathcal{C}^{\gamma}_{\text{lune}})). \end{aligned} \tag{49}$$

In particular it follows that each cycle $\mathcal{C}^{\gamma}_{\text{lune}}$ takes the same duration $T = 2n\pi/\Omega$ to be implemented, which has a favourable scaling $T \sim \pi/(2\Delta)$ with respect to the chemical shift difference of the spins. As discussed below, this property leads to efficient double-quantum excitation in the near-equivalence regime.

At this stage we'd like to point out that the trajectory in figure 4, and its associated geometric phase, only strictly applies when the detailed structure of each zero-quantum rotation is ignored. However we show in the supplementary material that the geometric picture in figure 4, and its associated geometric phase, may be recovered by using a suitable interaction frame, even when the detailed dynamics are taken into account giving a rigorous justification to our approach.

B. Spherical droplet

As a second example we consider a Bloch sphere trajectory tracing out the boundary of a spherical "droplet", defined as a combination of a spherical triangle with opening angle γ and half of a "spherical cap"[28] with apex angle γ (see figure 6). A spherical droplet trajectory may be generated by the following sequence of rotations

$$V^{\gamma}_{\text{drop}}(T) = R^{13}_{\gamma-\pi/2}(\pi/2)R^{13}_{\gamma/2}(\pi)R^{13}_{y}(\pi/2). \tag{50}$$

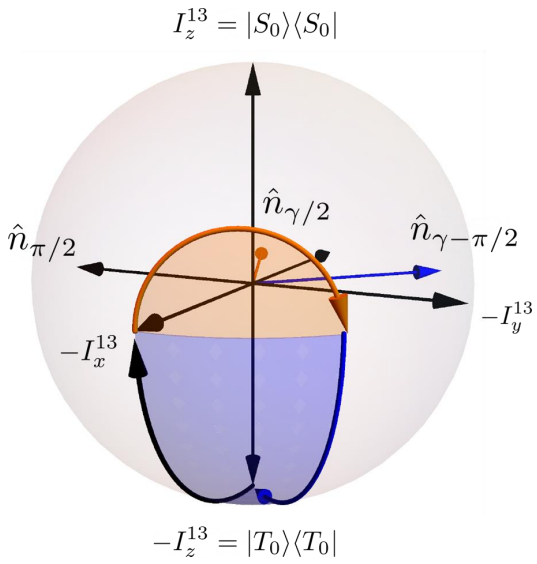

Figure 6. Bloch sphere trajectory in the $\{|S_0\rangle, |T_0\rangle\}$ subspace tracing out the boundary of a spherical droplet with opening angle $\gamma = \pi/4$ at the south pole. The initial $(\pi/2)_y$ rotation (black path) transforms the central triplet state into a singlet-triplet superposition state. A subsequent π rotation with phase $\phi = \gamma/2$ sweeps out the semicircular boundary of the half-cap (orange path). A final rotation through $\pi/2$ around a transverse axis with phase $\phi = \gamma - \pi/2$ completes the cycle (blue path).

The solid angle subtended by the spherical droplet with opening angle γ at the south pole is given by

$$\boldsymbol{\Omega}(\mathcal{C}^{\gamma}_{\text{drop}}) = \boldsymbol{\Omega}(\mathcal{C}^{\gamma}_{\text{tri}}) + \tfrac{1}{2}\boldsymbol{\Omega}(\mathcal{C}^{\gamma}_{\text{cap}}), \tag{51}$$

where $\boldsymbol{\Omega}(\mathcal{C}^{\gamma}_{\text{tri}}) = \gamma$ is the solid angle of a spherical triangle with opening angle γ and $\boldsymbol{\Omega}(\mathcal{C}^{\gamma}_{\text{cap}}) = \pi(1-\cos(\gamma/2))$ is the solid angle of a spherical cap with apex angle γ. It follows that the geometric phase for the cyclic trajectory of a spin-1/2 state which follows the boundary of the droplet is given by

$$\begin{aligned} \phi_{\text{geo}}(\mathcal{C}^{\gamma}_{\text{drop}}) &= \pm\tfrac{1}{2}(\boldsymbol{\Omega}(\mathcal{C}^{\gamma}_{\text{tri}}) + \tfrac{1}{2}\boldsymbol{\Omega}(\mathcal{C}^{\gamma}_{\text{cap}})) \\ &= \pm\tfrac{1}{2}(\gamma + \pi(1-\cos(\gamma/2))). \end{aligned} \tag{52}$$

As shown in the SI, the dynamic phase *does not* vanish for the cycle $\mathcal{C}^{\gamma}_{\text{drop}}$, but is instead given by

$$\phi_{\text{dyn}}(\mathcal{C}^{\gamma}_{\text{drop}}) = \pm\tfrac{1}{2}\pi\cos(\gamma/2). \tag{53}$$

The total phase is thus a combination of dynamic and geometric contributions

$$\begin{aligned} \phi_{\text{tot}}(\mathcal{C}^{\gamma}_{\text{drop}}) &= \pm\tfrac{1}{2}(\gamma+\pi) \\ &= \pm\tfrac{1}{2}(\boldsymbol{\Omega}(\mathcal{C}^{\gamma}_{\text{tri}}) + \pi), \end{aligned} \tag{54}$$

which may be seen to be sensitive to the solid angle of the subtended spherical triangle instead of the complete spherical droplet.

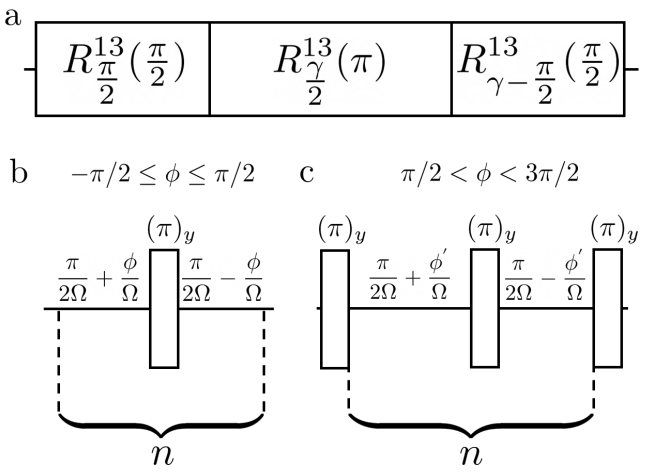

Figure 7. (a) Pulse sequence elements for generating a spherical droplet trajectory in the $\{|S_0\rangle, |T_0\rangle\}$ subspace, as shown in figure 6. This consists of a sequence of rotations in the zero-quantum subspace, where the implementation of each rotation $R^{13}_{\phi}(\xi)$ depends on its rotation angle ξ and phase angle ϕ, as follows: (b) If the phase ϕ of the effective rotation operator falls into the interval $[-\pi/2, +\pi/2]$, a rotation through an angle ξ is implemented by a sequence of n time-shifted echoes with the indicated timings, where n is chosen to satisfy $2n\theta_{\mathrm{ST}} \simeq \xi$. (c) If the phase ϕ of the effective rotation operator falls into the interval $(+\pi/2, +3\pi/2)$, a rotation through an angle ξ is implemented by a sequence of n time-shifted echoes with the indicated timings, where n is chosen to satisfy $2n\theta_{\mathrm{ST}} \simeq \xi$, and the time-shifted echo sequence is bracketed by two π_y pulses.

The spherical droplet trajectory may be implemented by a series of time-shifted spin echo blocks as indicated in figure 7a. It is convenient to employ rotation phases lying on the right half of the unit circle ($\phi \in [-\pi/2, +\pi/2]$). To cover the whole unit circle we replace effective rotations with phase $\pi/2 < \phi < 3\pi/2$ by a time-shifted spin echo block with rotation phase $\phi - \pi$ sandwiched between two 180° pulses (see figure 7b). With this in mind, the first echo block is chosen to generate an effective rotation with phase $\phi = \pi/2$, the second spin echo block is chosen to generate an effective rotation with phase $\phi = \gamma/2$, and the last spin echo block is chosen to generate an effective rotation with phase $\phi = \gamma - \pi/2$. In all cases the echo number is chosen to satisfy

$$2n\theta_{\mathrm{ST}} \simeq \pi/2, \tag{55}$$

leading to an approximate $\pi/2$ rotation for the first and last echo block, and an approximate π rotation for the central echo block.

The total phase given by equation 54 indicates that the propagator for the cycle $\mathcal{C}^{\gamma}_{\mathrm{drop}}$ may be expressed as shown below

$$V^{\gamma}_{\mathrm{drop}}(T) = R^{13}_{z}(\pi + \mathbf{\Omega}(\mathcal{C}^{\gamma}_{\mathrm{tri}})), \tag{56}$$

with no net effect on the outer triplet states. The observed spectral intensity is then given by

$$\langle S^{\gamma}_{\mathrm{drop}}(\omega)\rangle \propto \cos(\mathbf{\Omega}(\mathcal{C}^{\gamma}_{\mathrm{tri}})/2 + \pi/2) = -\sin(\mathbf{\Omega}(\mathcal{C}^{\gamma}_{\mathrm{tri}})/2). \tag{57}$$

The last expression highlights two interesting facts. Firstly, the observed NMR signal for the spherical drop only depends on the surface area of the enclosed spherical triangle. As a consequence the observed NMR signal returns to its original value whenever the surface area of the spherical triangle equals 4π. In addition, the NMR signal displays a surface area offset of $\pi/2$ when compared to the spherical lune experiment leading to a sine dependence rather than a cosine dependence. The NMR signal in an interferometry experiment is therefore expected to vanish at $\gamma = 0$ and then increase with increasing surface area of the spherical triangle.

VI. EXPERIMENTAL

A. Sample

All experiments were performed on a 30 mM solution of a $^{13}C_2$-labelled deutero-alkoxy naphthalene derivative ($^{13}C_2$-DAND) dissolved in 500 μL isopropanol-d_8, contained in a standard Wilmad 5 mM sample tube without deoxygenation of the sample. The synthesis of $^{13}C_2$-DAND is described in reference 36. The molecular structure and relevant NMR parameters are given in table I. The two ^{13}C sites have a J-coupling of 54.39±0.10 Hz and a chemical shift difference of 7.50±0.2 Hz in the operating magnetic field of 9.39 T. This leads to an effective frequency of 54.04 Hz and a singlet-triplet mixing angle of 7.85° as defined in equations 20 and 21.

Table I. Chemical structure of 1,2,3,4,5,6,8-heptakis-(methoxy-d_3)-7-((propan-2-yl-d_7)oxy)-naphthalene-4a,8a-[$^{13}C_2$]. Relevant NMR parameters are given for a magnetic field strength of 9.39 T.

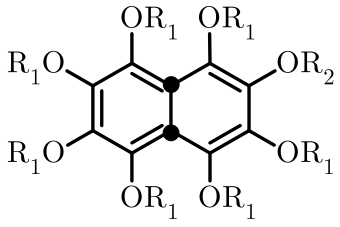

J/Hz	54.39 ± 0.10
$\Delta\delta$/ppb	75.0 ± 2.0
$\omega_{\Delta}/(2\pi)$/Hz [@9.39 T]	7.50 ± 0.20
$\Omega/(2\pi)$/Hz	54.04 ± 0.10
θ_{ST}/°	7.85 ± 0.22

$\omega_{\mathrm{nut}}/(2\pi)$	25 kHz
τ_{90}	10 μs
π/Ω	9190 μs
$\pi/(2\Omega)$	4595 μs
$3\pi/(2\Omega)$	13785 μs
n	12

Table II. Experimental parameters for the spherical lune experiment shown in figure 5. Here, ω_{nut} refers to the radiofrequency pulse amplitude, expressed as a nutation frequency; τ_{90} is the duration of a 90° pulse, Ω refers to the effective frequency of the system in rad s^{-1}, and n refers to the repetition number of the TSSE blocks.

B. NMR

1. Equipment

The magnetic field of 9.39 T was provided by a wide-bore Oxford 400 magnet. The data was acquired using a Bruker AVANCE NEO console equipped with a 5 mm multinuclear Bruker BBO probe (^{1}H/D/X).

2. Interferometry

Spherical lune. NMR interferometry experiments for the spherical lune were performed according to figure 5 with the pulse sequence parameters given in table II. Throughout the experiment the echo number was fixed to $n = 12$. The rotation phase of the second TSSE block was varied throughout the experiment in agreement with equation 41 to generate a set of opening angles γ. Variations of the rotation phase for the spherical lune experiment were performed in the following manner:

1. For a given opening angle γ determine the rotation phase of the second TSSE block through $\phi = \gamma - \pi/2$.
2. If the phase satisfies $-\pi/2 \leq \phi \leq +\pi/2$ use the pulse sequence shown in figure 5a.
3. If the phase satisfies $+\pi/2 < \phi < 3\pi/2$ use the pulse sequence shown in figure 5b.

Following the above protocol we measured the geometric phase for opening angles γ ranging from 0° to 360° in increments of 5°.

Spherical Droplet. NMR interferometry experiments for the spherical droplet were performed according to figure 7 with the pulse sequence parameters given in table III. Throughout the experiment the echo number was fixed to $n = 6$. Following figure 7a the rotation phase for the first TSSE block was kept fixed at $\phi_1 = \pi/2$. Since ϕ_1 falls into the interval $-\pi/2 \leq \phi_1 \leq +\pi/2$ the first TSSE block was implemented with the pulse sequence element shown in figure 7b. The rotation phase ϕ_2 for the second TSSE block and the rotation phase ϕ_3 for the third TSSE block were varied throughout the experiment in agreement with equation 50 to generate a set of opening angles γ. Variations of the rotation phases ϕ_2 and ϕ_3 were performed in the following manner:

1. For a given opening angle γ determine the rotation phase ϕ_2 through $\phi_2 = \gamma/2$.
2. If ϕ_2 satisfies $-\pi/2 \leq \phi_2 \leq +\pi/2$ use the TSSE block shown in figure 7b with $\phi = \phi_2$.
3. If ϕ_2 satisfies $+\pi/2 < \phi_2 < +3\pi/2$ use the TSSE block shown in figure 7c with $\phi^{'} = \phi_2 - \pi$.
4. Determine the rotation phases ϕ_3 through $\phi_3 = \gamma - \pi/2$.
5. If ϕ_3 satisfies $-\pi/2 \leq \phi_3 \leq +\pi/2$ use the TSSE block shown in figure 7b with $\phi = \phi_3$.
6. If ϕ_3 satisfies $+\pi/2 < \phi_3 < +3\pi/2$ use the TSSE block shown in figure 7c with $\phi^{'} = \phi_3 - \pi$.

Following the above protocol we measured the geometric phase for opening angles γ ranging from 0° to 360° in increments of 5°.

$\omega_{\mathrm{nut}}/(2\pi)$	25 kHz
τ_{90}	10 μs
π/Ω	9190 μs
$\pi/(2\Omega)$	4595 μs
n	6

Table III. Experimental parameters for the spherical droplet experiment shown in figure 7. Here, ω_{nut} refers to the radiofrequency pulse amplitude, expressed as a nutation frequency, τ_{90} is the duration of a 90° pulse; Ω refers to the effective frequency of the system in rad s^{-1}, and n refers to the repetition number of the TSSE block.

3. Double-quantum NMR

Double-quantum excitation experiments followed the acquisition strategy outlined in figure 8a. Double-quantum coherences are initially excited via the pulse block element DQ starting from thermal z-magnetization. Excited double-quantum coherences are subsequently reconverted into magnetization via application of a second pulse block element DQ. A final 90° pulse induces the observation of the free induction decay. To filter out spin density operator components that have passed through double-quantum terms after the first excitation block we employed a standard four-step phase cycle[29,30] as explained in section III C. The double-quantum excitation blocks DQ were given by a

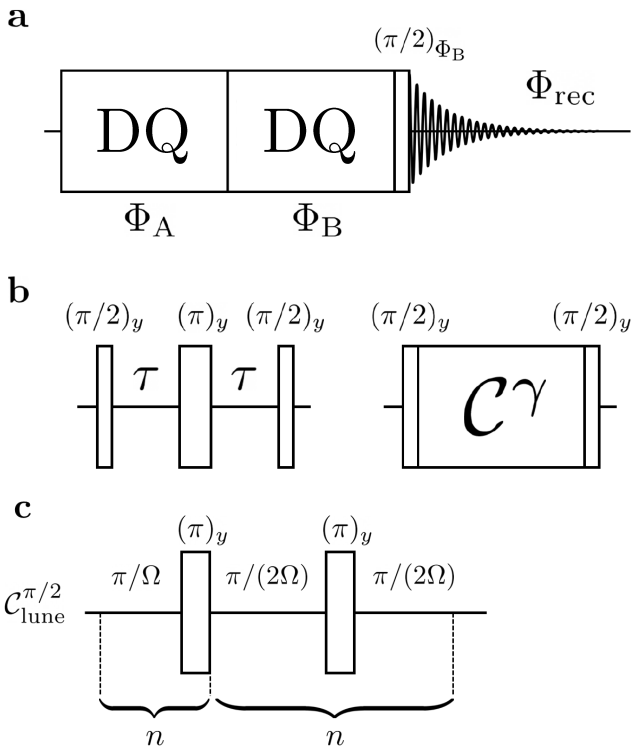

Figure 8. Double-quantum pulse sequences. (a) Generic double-quantum filtered acquisition scheme. (b) Double-quantum excitation schemes. Left: a standard INADEQUATE sequence[25,29,30]. Right: a geometric double-quantum excitation scheme consisting of a cycle $\mathcal{C}_{\text{geo}}$ sandwiched between two 90° pulses along a common axis. The cycle $\mathcal{C}_{\text{geo}}$ confers a geometric phase on the zero-quantum states. (c) Implementation of the cycle $\mathcal{C}_{\text{geo}} = \mathcal{C}^{\pi/2}_{\text{lune}}$ for a spherical lune with opening angle $\gamma = \pi/2$. The echo number is chosen to satisfy $2n\theta_{\text{ST}} = \pi$. Explicit timing parameters for the current case are given in table V.

standard INADEQUATE sequence or a geometric excitation scheme as shown in figure 8b.

The half-echo duration τ_{DQ} for the INADEQUATE block was optimised experimentally over a window centered around the theoretically optimal value $\tau_{\text{opt}} = \pi/(4\Omega\sin^2(\frac{1}{2}\theta_{\text{ST}}))$ for nearly-equivalent spin-pairs[27] with the parameters given in table I. The optimised experimental parameters for the INADEQUATE experiment are summarised in table IV.

A geometric excitation scheme based on a spherical lune experiment is shown in figure 8c. This sequence generates the cycle $\mathcal{C}^{\pi/2}_{\text{lune}}$ with the experimental parameters given in table V.

$\omega_{\text{nut}}/(2\pi)$	25 kHz
τ_{90}	10 μs
τ_{DQ}	375 ms

Table IV. Experimentally optimised pulse sequence parameters for the double-quantum filtered INADEQUATE experiment shown in figure 8. ω_{nut} refers to the radiofrequency pulse amplitude, τ_{90} is the duration of a 90° pulse, and τ_{DQ} refers to the half-echo duration of the INADEQUATE spin echo.

$\omega_{\text{nut}}/(2\pi)$	25 kHz
τ_{90}	10 μs
π/Ω	9190 μs
$\pi/(2\Omega)$	4595 μs
n	12

Table V. Experimental parameters for the double-quantum filtered spherical lune experiment shown in figure 8c, for the opening angle $\gamma = \pi/2$, leading to optimal geometric double-quantum excitation. ω_{nut} refers to the radiofrequency pulse amplitude expressed as a nutation frequency, τ_{90} is the duration of a 90° pulse, Ω refers to the effective frequency of the system in $\text{rad}\,\text{s}^{-1}$, and n refers to the repetition number of the TSSE blocks.

VII. RESULTS

A. NMR Interferometry

Figure 9 shows ^{13}C NMR signal amplitudes for the $^{13}C_2$-DAND solution in the interferometry experiment of figure 1(a), where the cycle $\mathcal{C}$ generates the spherical lune zero-quantum trajectory shown in figure 4, and which is implemented by applying the pulse sequence shown in figure 5.

The signal amplitudes are acquired by varying the opening angle γ of the lune, which leads in turn to a variation of the solid angle $\mathbf{\Omega}(\mathcal{C}^{\gamma}_{\text{lune}})$, through equation 42. As explained in section IV, to cover the whole unit circle it is necessary to make use of the two resonance conditions $\tau_{\pm}$. The left half of the data set (orange shaded region) has been acquired using the τ_+ condition utilising the pulse sequence shown in figure 5a, whereas the right half of the data set (green shaded region) has been obtained using the τ_- condition utilising the pulse sequence shown in figure 5b.

In full agreement with equation 48 the signal amplitude follows a cosine curve as a function of the solid angle subtended by the spherical lune trajectory. A complete signal recovery is achieved for a cycle with a solid angle of $\mathbf{\Omega}(\mathcal{C}^{\pi}_{\text{lune}}) = 4\pi$ indicating the invariance of the fictitious $\{|S_0\rangle, |T_0\rangle\}$ two-level system to a 4π rotation.

Figure 10 shows ^{13}C NMR signal amplitudes for the spherical droplet sequence (figure 7) as a function of the

Accepted to J. Chem. Phys. 10.1063/5.0138146

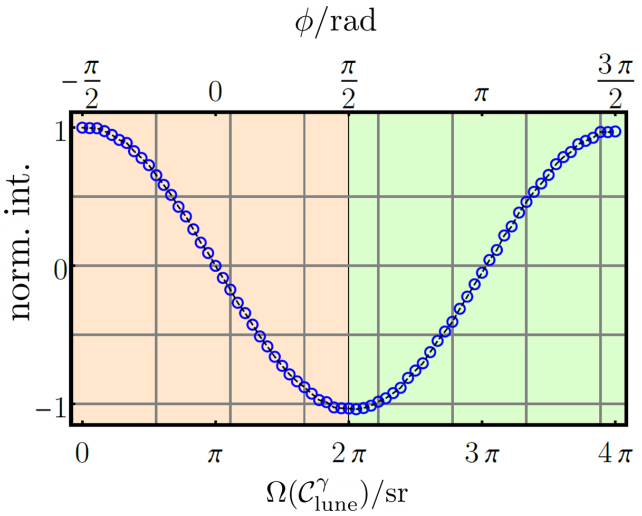

Figure 9. Experimental ^{13}C signal amplitudes (blue dots) for the spherical lune sequence shown in figure 5 as a function of the solid angle subtended by the spherical lune $\mathbf{\Omega}(\mathcal{C}^{\gamma}_{\text{lune}})$. Throughout the experiment the rotation phase ϕ of the second TSSE block has been varied to adjust the opening angle of the lune (top horizontal axis). As indicated in figure 3 the whole unit circle is covered by exploiting the two resonance conditions $\tau_{\pm}$. Data points in the orange shaded region were acquired with τ_{+} resonance condition utilising the pulse sequence shown in figure 5a. Data points in the green shaded region were acquired with τ_{-} resonance condition utilising the pulse sequence shown in figure 5b. The signal amplitudes are normalized relative to the maximum signal of the data series.

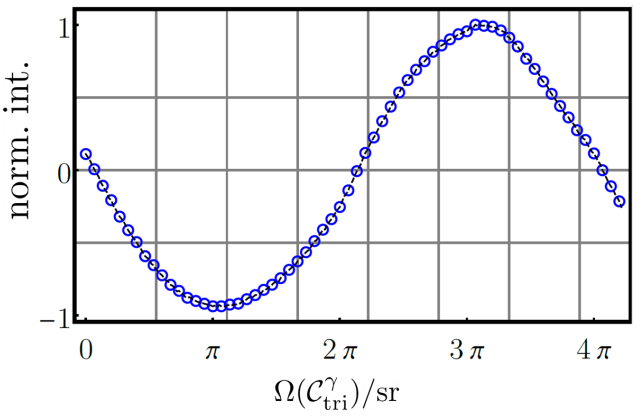

Figure 10. Experimental ^{13}C signal amplitudes (blue dots) for the spherical droplet sequence shown in figure 7 as a function of the solid angle subtended by the spherical triangle $\mathbf{\Omega}(\mathcal{C}^{\gamma}_{\text{tri}})$. The signal amplitudes are normalized relative to the maximum signal of the data series.

	90°	INADEQUATE	$\mathcal{C}^{\pi/2}_{\text{lune}}$
norm. int.	1	0.36	0.73

Table VI. Integrated signal amplitudes for the double-quantum filtered spectra shown in figure 11. The amplitudes are normalised with respect to the 90° reference spectrum.

solid angle subtended by the the enclosed spherical triangle.

In agreement with equation 57 the observed NMR signal for the spherical droplet follows a sine curve rather than a cosine curve. Additionally, the observed signal amplitudes clearly display a half period of 2π when plotted against the solid angle $\mathbf{\Omega}(\mathcal{C}^{\gamma}_{\text{tri}})$ of the spherical triangle enclosed by the cycle $\mathcal{C}^{\gamma}_{\text{drop}}$. As expected, a full recovery of the initial signal occurs for a cycle which displays a solid angle of $\mathbf{\Omega}(\mathcal{C}^{\gamma}_{\text{tri}}) = 4\pi$ for the spherical triangle swept out in the process.

The signal does not start out exactly at zero as suggested by equation 57, but is slightly shifted. We attribute this small discrepancy to second order effects in the mixing angle θ_{ST}.

B. Geometric double-quantum excitation

To examine the efficiency of geometric double-quantum excitation we performed double-quantum-filtering experiments according to the scheme in figure 8. A comparison of double-quantum-filtered signals obtained by the standard INADEQUATE experiment and by geometric double-quantum excitation using a spherical lune with opening angle $\gamma = \pi/2$ is shown in figure 11. A 90°-pulse acquire spectrum averaged over four transients is given as a reference.

Integrated signal amplitudes normalised with respect to the integrated signal amplitude of the reference spectrum are given in table VI. The geometric double-quantum excitation scheme retains approximately 73% percent of the original magnetization, whereas the INADEQUATE sequence only retains about 36% percent of the original magnetization. The geometric double-quantum excitation scheme therefore outperforms the INADEQUATE sequence by a factor of two in this particular case.

We attribute this increase in performance to the much faster excitation of double-quantum coherences for the geometric schemes, compared to the conventional INADEQUATE method. In the current case, the total double-quantum excitation time for the geometric cycle $\mathcal{C}^{\pi/2}_{\text{lune}}$ is given by $T^{\text{geo}}_{\text{DQ}} \simeq 220.56$ ms. The experimentally optimized double-quantum excitation time T_{DQ} for the INADEQUATE sequence, on the other hand, is given by $T^{\text{INDQ}}_{\text{DQ}} \simeq 750$ ms. The geometric scheme therefore excites double-quantum coherences more than three times faster than the INADEQUATE sequence, considerably reducing the losses due to T_2 relaxation.

We have checked by experiment and simulation that the geometric double-quantum excitation sequences are very robust with respect to resonance offset, in the case

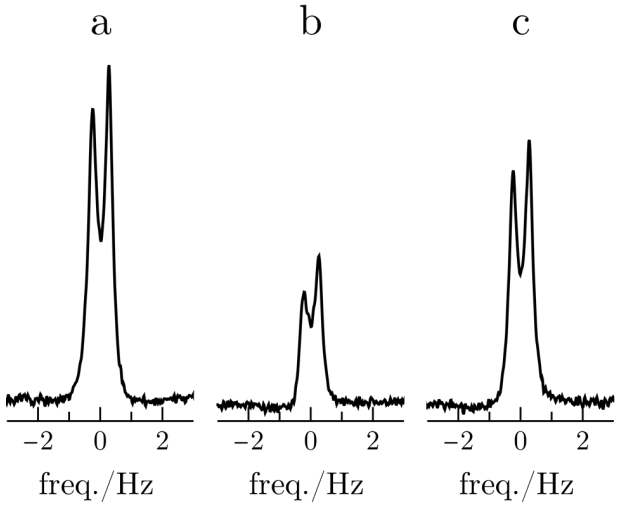

Figure 11. ^{13}C spectra obtained after (a) a single 90° pulse averaged over 4 transients, (b-c) after double-quantum filtering the ^{13}C NMR signal according to the strategy outlined in figure 8. (a) Standard ^{13}C spectrum obtained with a single 90° pulse. (b) Double-quantum filtered spectrum obtained with the standard INADEQUATE pulse sequence, using the experimentally optimized pulse sequence parameters given in table IV. (c) Double-quantum filtered spectrum obtained by geometric double-quantum excitation, using the cycle $\mathcal{C}^{\pi/2}_{\text{lune}}$, leading to a solid angle of $\boldsymbol{\Omega}(\mathcal{C}) = \pi$ for the spherical lune. The experimental pulse sequence parameters are given in table V.

that the number of echoes n is an even number.

VIII. SUMMARY

The Aharonov-Anandan phase applies to any cyclic evolution of a quantum state, as opposed to the better-known Berry's phase, which only applies to adiabatic transformations[1,2]. Indeed, the Aharonov-Anandan phase may be regarded as a generalization of Berry's phase, with the two expressions converging in the case of adiabatic transformations. Since magnetic resonance experiments often use non-adiabatic transformations, the Aharonov-Anandan phase deserves to be better known by magnetic resonance spectroscopists. Despite this, the authors are not aware of any experimental exploitations of the Aharonov-Anandan phase in the context of nuclear magnetic resonance spectroscopy going beyond elementary demonstrations[6].

In this work we have demonstrated NMR interferometry experiments involving the zero-quantum subspace of near-equivalent spin-1/2 pairs. A cyclic trajectory in the zero-quantum subspace confers opposite phase factors on the two triplet-triplet coherences which contribute to the NMR signal. The phase factor is the sum of a dynamic and a geometric term. The interferometry experiments are in full agreement with theoretical predictions, providing that the geometric Aharonov-Anandan phase is taken into account. Pulse sequences are described which generate arbitrary Aharonov-Anandan phases for cyclic trajectories in the zero-quantum subspace. In the case of the spherical lune trajectory, the dynamic phase contribution vanishes, so that the interferometry experiment gives a direct read-out of the geometric phase.

We have also demonstrated a practical application of the Aharonov-Anandan phase. Double-quantum excitation is an important feature of many modern NMR experiments, and is used for a variety of purposes including the removal of undesirable signals from NMR spectra[20,37], for aiding spectral assignment[21,37], and for exploring cross-correlated relaxation processes[22–24]. Although double-quantum excitation is routine for weakly coupled systems in solution NMR, it is much more difficult to achieve with good efficiency for strongly coupled systems, especially in the limit of near-equivalence. We have shown that this problem may be addressed by exploiting the geometric Aharonov-Anandan phase. In the case under investigation, the efficiency of a double-quantum-filtering experiment is more than doubled for near-equivalent spin pairs by exploiting the geometric Aharonov-Anandan phase.

One application of geometric double-quantum filtration could be to identify near-equivalent $^{13}C_2$ spin pairs in natural abundance, and to measure their singlet lifetimes[38]. Efficient double-quantum excitation should facilitate such studies, in the case of near-equivalent spin pairs.

IX. SUPPLEMENTARY MATERIAL

The supplementary material includes further details on the analytic calculations given in sections IV, V, as well as information on the geometric phase when taking the detailed dynamics of the system into account.

ACKNOWLEDGEMENTS

This research was supported by the European Research Council (grant 786707-FunMagResBeacons) and the EPSRC-UK (grant EP/V055593/1).

AUTHOR DECLARATIONS

Conflict of interest

The authors have no conflicts to disclose.

DATA AVAILABILITY STATEMENT

The pulse sequences used for the experiments described in this paper, as well as detailed Mathematica notebooks

supporting calculations in sections IV, V and the supplementary material have been deposited on the open-access repository `eprints.soton.ac.uk` and may be accessed via `doi:10.5258/SOTON/D2517`. The experimental data are available from the authors at reasonable request.

REFERENCES

[1] M. V. Berry, Proceedings of the Royal Society of London. Series A, Mathematical and Physical Sciences **392**, 45 (1984).
[2] Y. Aharonov and J. Anandan, Physical Review Letters **58**, 1593 (1987).
[3] M. E. Stoll, A. J. Vega, and R. W. Vaughan, Physical Review A **16**, 1521 (1977).
[4] D. Suter, G. C. Chingas, R. A. Harris, and A. Pines, Molecular Physics **61**, 1327 (1987).
[5] R. Tycko, Physical Review Letters **58**, 2281 (1987).
[6] D. Suter, K. T. Mueller, and A. Pines, Physical Review Letters **60**, 1218 (1988).
[7] J. Du, P. Zou, M. Shi, L. C. Kwek, J.-W. Pan, C. H. Oh, A. Ekert, D. K. L. Oi, and M. Ericsson, Physical Review Letters **91**, 100403 (2003).
[8] T. Gopinath and A. Kumar, Physical Review A **73**, 022326 (2006).
[9] A. Ghosh and A. Kumar, Physics Letters A **349**, 27 (2006).
[10] J. Du, J. Zhu, M. Shi, X. Peng, and D. Suter, Physical Review A **76**, 042121 (2007).
[11] X. Peng, S. Wu, J. Li, D. Suter, and J. Du, Physical Review Letters **105**, 240405 (2010).
[12] M. Carravetta, O. G. Johannessen, and M. H. Levitt, Physical Review Letters **92**, 153003 (2004).
[13] G. Pileio, M. Carravetta, and M. H. Levitt, Proceedings of the National Academy of Sciences **107**, 17135 (2010).
[14] M. C. D. Tayler and M. H. Levitt, Physical Chemistry Chemical Physics **13**, 5556 (2011).
[15] G. Stevanato, J. T. Hill-Cousins, P. Håkansson, S. S. Roy, L. J. Brown, R. C. D. Brown, G. Pileio, and M. H. Levitt, Angewandte Chemie International Edition **54**, 3740 (2015).
[16] M. H. Levitt, Journal of Magnetic Resonance **306**, 69 (2019).
[17] G. Pileio, ed., *Long-Lived Nuclear Spin Order: Theory and Applications*, 1st ed. (Royal Society of Chemistry, S.l., 2020).
[18] A. M. R. Hall, T. A. A. Cartlidge, and G. Pileio, Journal of Magnetic Resonance **317**, 106778 (2020).
[19] C. Bengs, L. Dagys, G. A. I. Moustafa, J. W. Whipham, M. Sabba, A. S. Kiryutin, K. L. Ivanov, and M. H. Levitt, The Journal of Chemical Physics **155**, 124311 (2021).
[20] A. Bax, R. Freeman, and S. P. Kempsell, Journal of the American Chemical Society **102**, 4849 (1980).
[21] A. Bax, R. Freeman, T. A. Frenkiel, and M. H. Levitt, J. Magn. Reson. **43**, 478 (1981).
[22] A. Wokaun and R. Ernst, Molecular Physics **36**, 317 (1978).
[23] S. Ravindranathan, X. Feng, T. Karlsson, G. Widmalm, and M. H. Levitt, Journal of the American Chemical Society **122**, 1102 (2000).
[24] B. Reif, A. Diener, M. Hennig, M. Maurer, and C. Griesinger, Journal of Magnetic Resonance **143**, 45 (2000).
[25] A. Bax, R. Freeman, and S. P. Kempsell, Journal of Magnetic Resonance (1969) **41**, 349 (1980).
[26] T. Nakai and C. A. McDowell, Molecular Physics **79**, 965 (1993).
[27] C. Bengs, *Non-Equilibrium Nuclear Spin States*, Ph.D. thesis, University of Southampton (2020).
[28] A. N. Pressley, *Elementary Differential Geometry*, 2nd ed. (Springer, London ; New York, 2010).
[29] M. H. Levitt, *Spin Dynamics: Basics of Nuclear Magnetic Resonance* (Wiley, 2001).
[30] J. Keeler, *Understanding NMR Spectroscopy*, 2nd ed. (Wiley, Chichester, U.K, 2010).
[31] M. C. D. Tayler and M. H. Levitt, Journal of the American Chemical Society **135**, 2120 (2013).
[32] A. Wokaun and R. R. Ernst, The Journal of Chemical Physics **67**, 1752 (1977).
[33] S. Vega, The Journal of Chemical Physics **68**, 5518 (1978).
[34] C. Bengs, M. Sabba, A. Jerschow, and M. H. Levitt, Physical Chemistry Chemical Physics **22**, 9703 (2020).
[35] M. Sabba, N. Wili, C. Bengs, J. W. Whipham, L. J. Brown, and M. H. Levitt, The Journal of Chemical Physics **157**, 134302 (2022).
[36] J. T. Hill-Cousins, I.-A. Pop, G. Pileio, G. Stevanato, P. Håkansson, S. S. Roy, M. H. Levitt, L. J. Brown, and R. C. D. Brown, Organic Letters **17**, 2150 (2015).
[37] M. Rance, O. W. Sørensen, G. Bodenhausen, G. Wagner, R. R. Ernst, and K. Wüthrich, Biochemical and Biophysical Research Communications **117**, 479 (1983).
[38] K. Claytor, T. Theis, Y. Feng, and W. Warren, Journal of Magnetic Resonance **239**, 81 (2014).

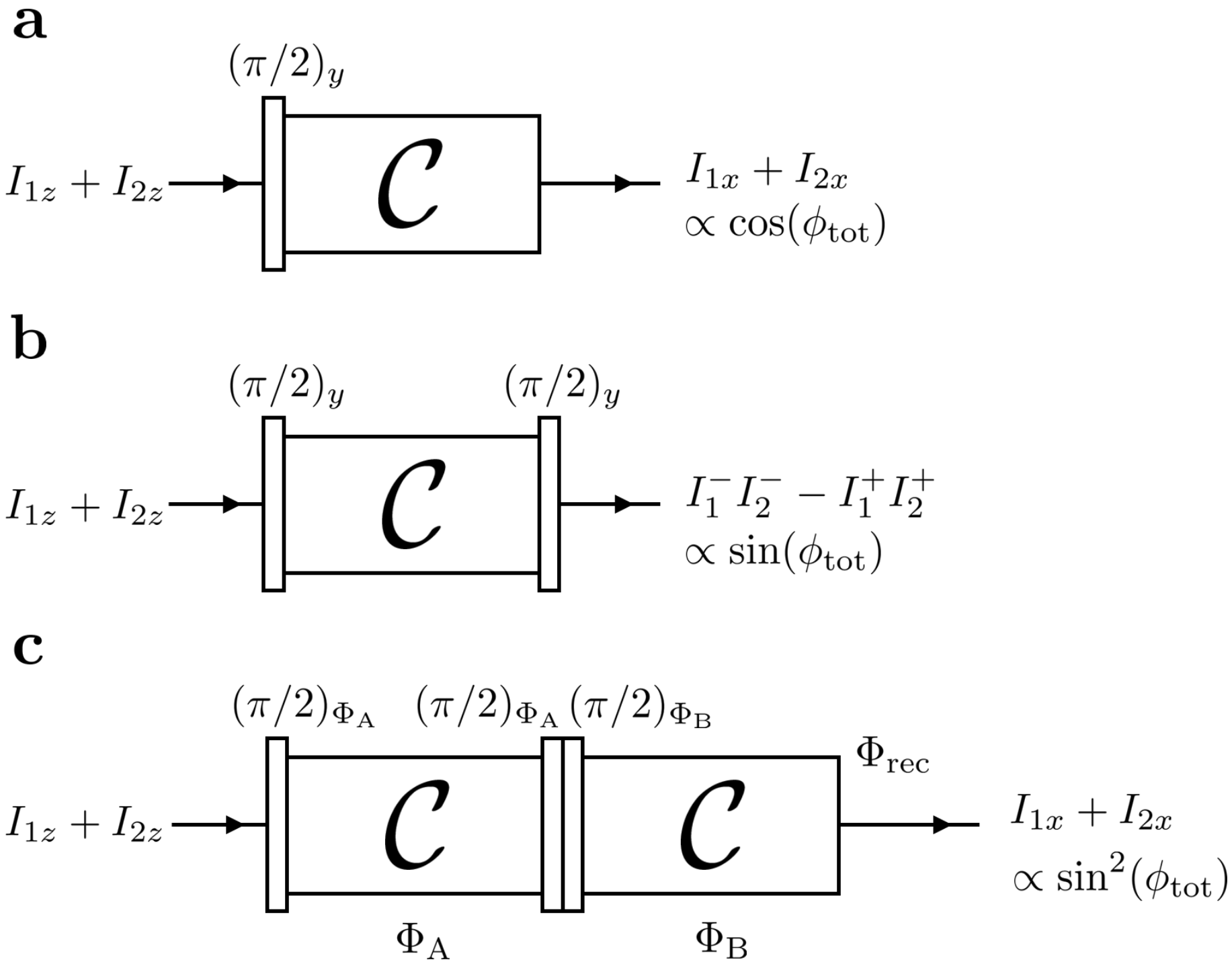
a
$(\pi/2)_y$
$I_{1z} + I_{2z}$
$\mathcal{C}$
$I_{1x} + I_{2x}$
$\propto \cos(\phi_{\mathrm{tot}})$
b
$(\pi/2)_y$
$(\pi/2)_y$
$I_{1z} + I_{2z}$
$\mathcal{C}$
$I_1^- I_2^- - I_1^+ I_2^+$
$\propto \sin(\phi_{\mathrm{tot}})$
c
$(\pi/2)_{\Phi_\mathrm{A}}$
$(\pi/2)_{\Phi_\mathrm{A}}$
$(\pi/2)_{\Phi_\mathrm{B}}$
Φ_{rec}
$I_{1z} + I_{2z}$
$\mathcal{C}$
$\mathcal{C}$
$I_{1x} + I_{2x}$
$\propto \sin^2(\phi_{\mathrm{tot}})$
Φ_A
Φ_B

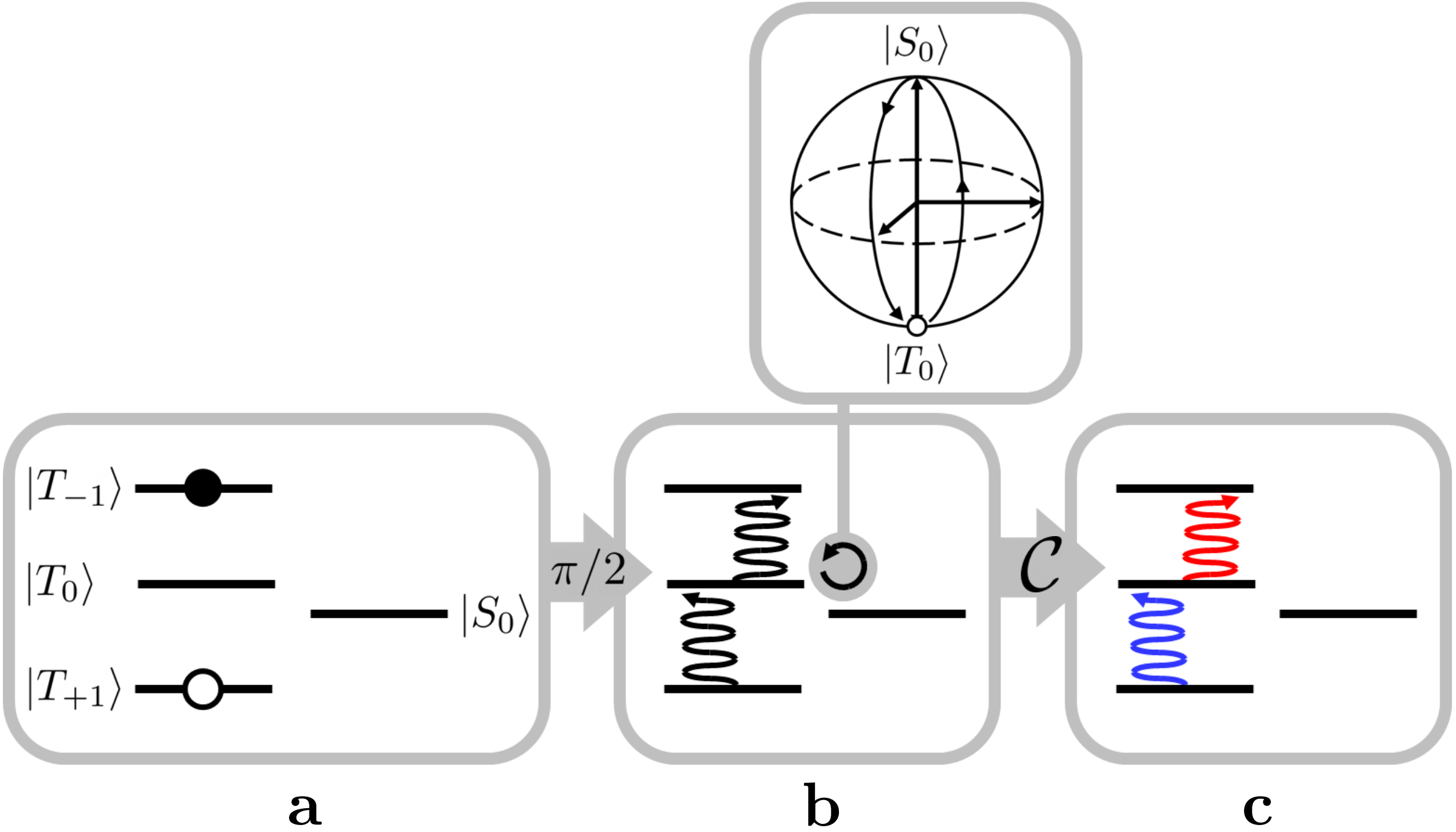
$|S_0\rangle$
$|T_0\rangle$
$|T_{-1}\rangle$
$|T_0\rangle$
$|T_{+1}\rangle$
$|S_0\rangle$
$\pi/2$
C
a
b
c

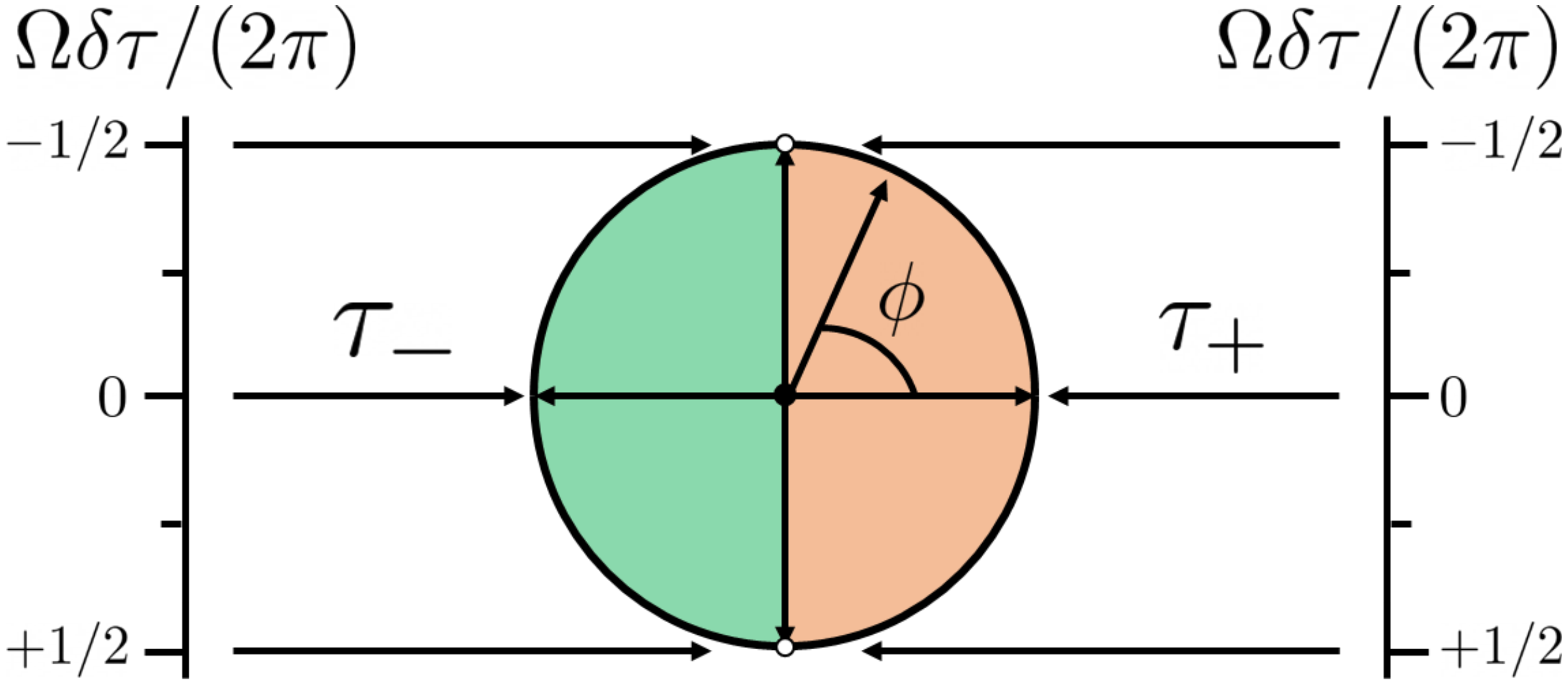
$\Omega\delta\tau/(2\pi)$
$\Omega\delta\tau/(2\pi)$
$-1/2$
0
$+1/2$
τ_-
ϕ
τ_+
$-1/2$
0
$+1/2$

$$I_z^{13} = |S_0\rangle\langle S_0|$$

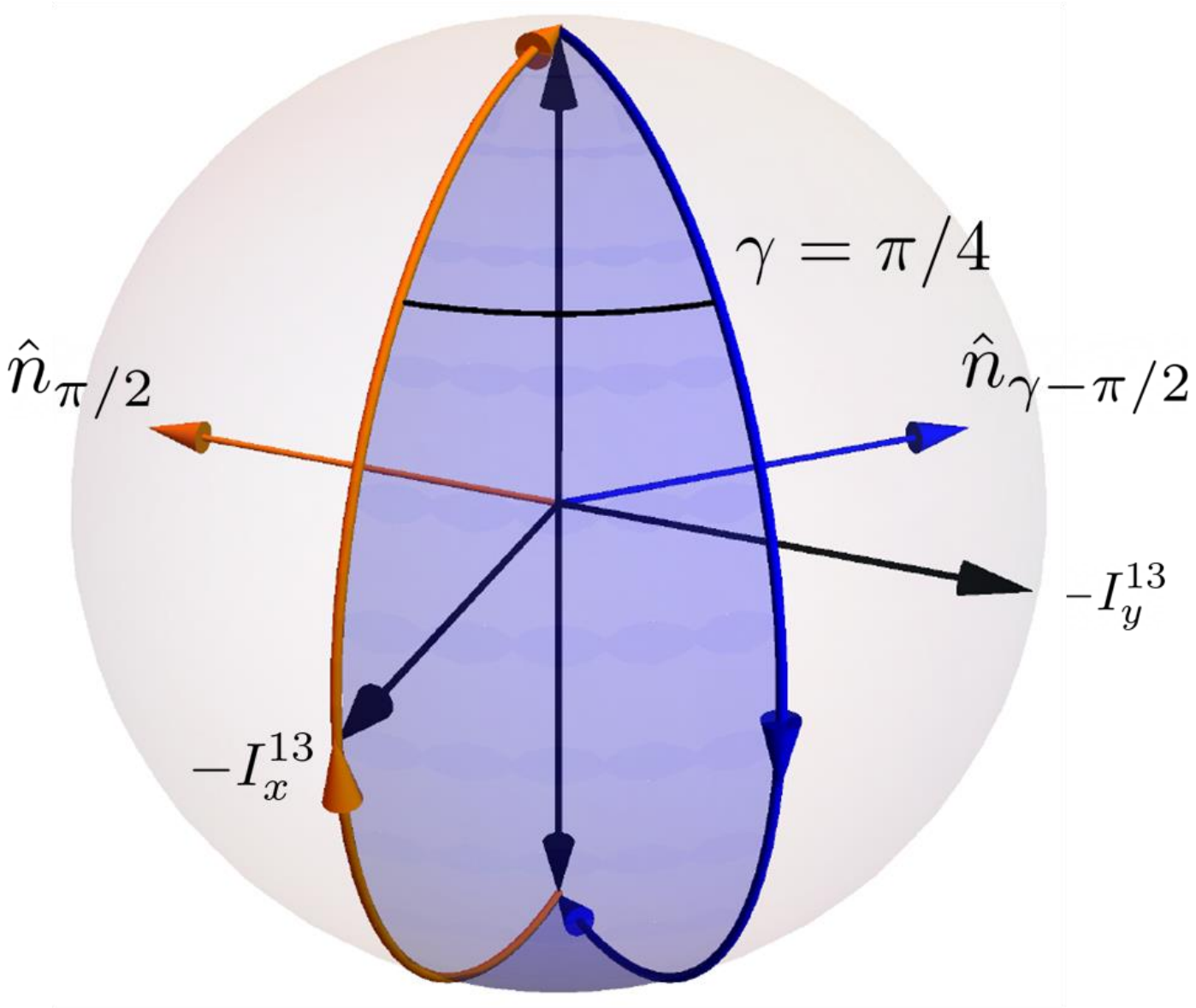

$$-I_z^{13} = |T_0\rangle\langle T_0|$$

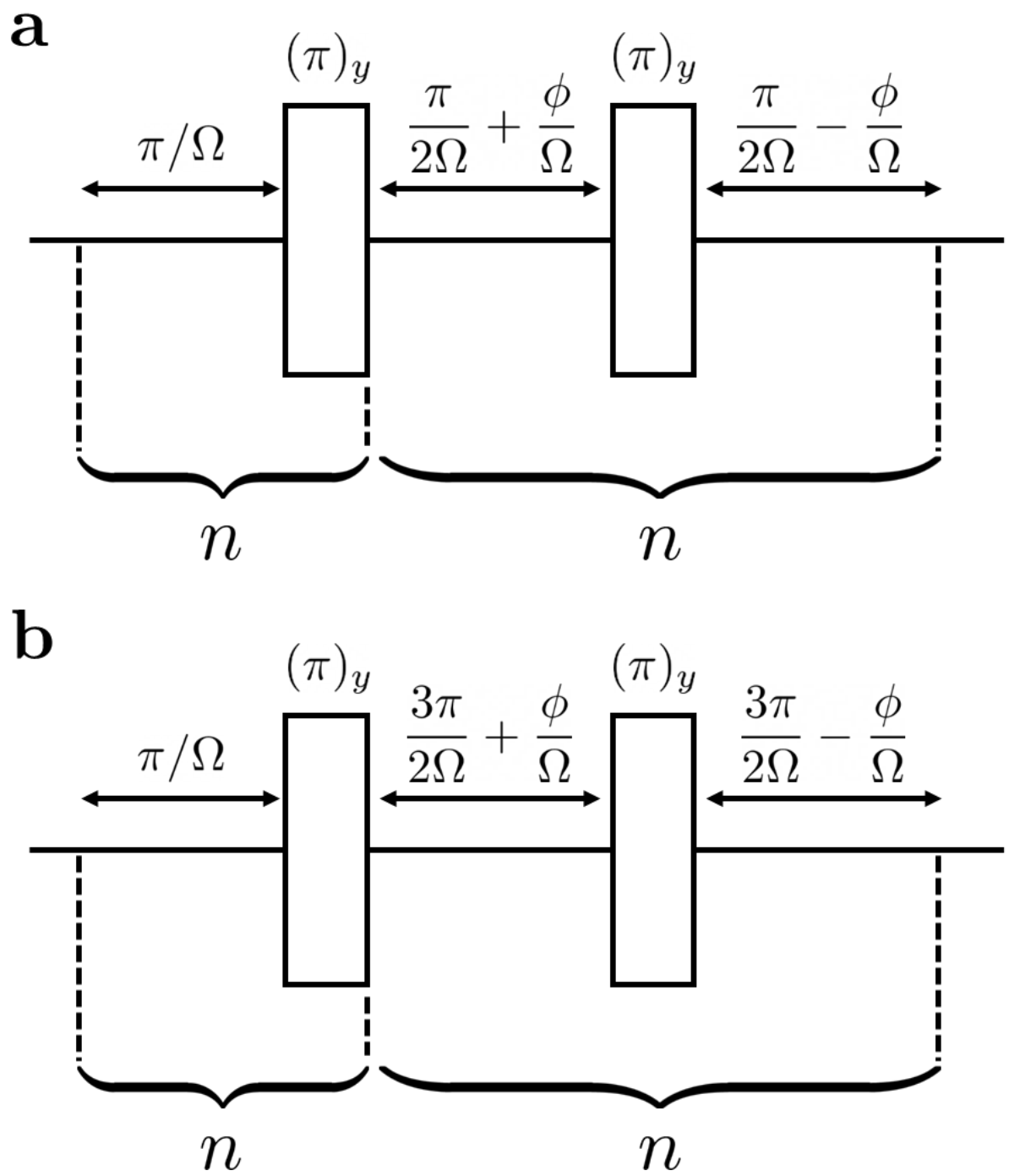
a
$(\pi)_y$
$(\pi)_y$
π/Ω
$\frac{\pi}{2\Omega} + \frac{\phi}{\Omega}$
$\frac{\pi}{2\Omega} - \frac{\phi}{\Omega}$
n
n
b
$(\pi)_y$
$(\pi)_y$
π/Ω
$\frac{3\pi}{2\Omega} + \frac{\phi}{\Omega}$
$\frac{3\pi}{2\Omega} - \frac{\phi}{\Omega}$
n
n

$$I_z^{13} = |S_0\rangle\langle S_0|$$

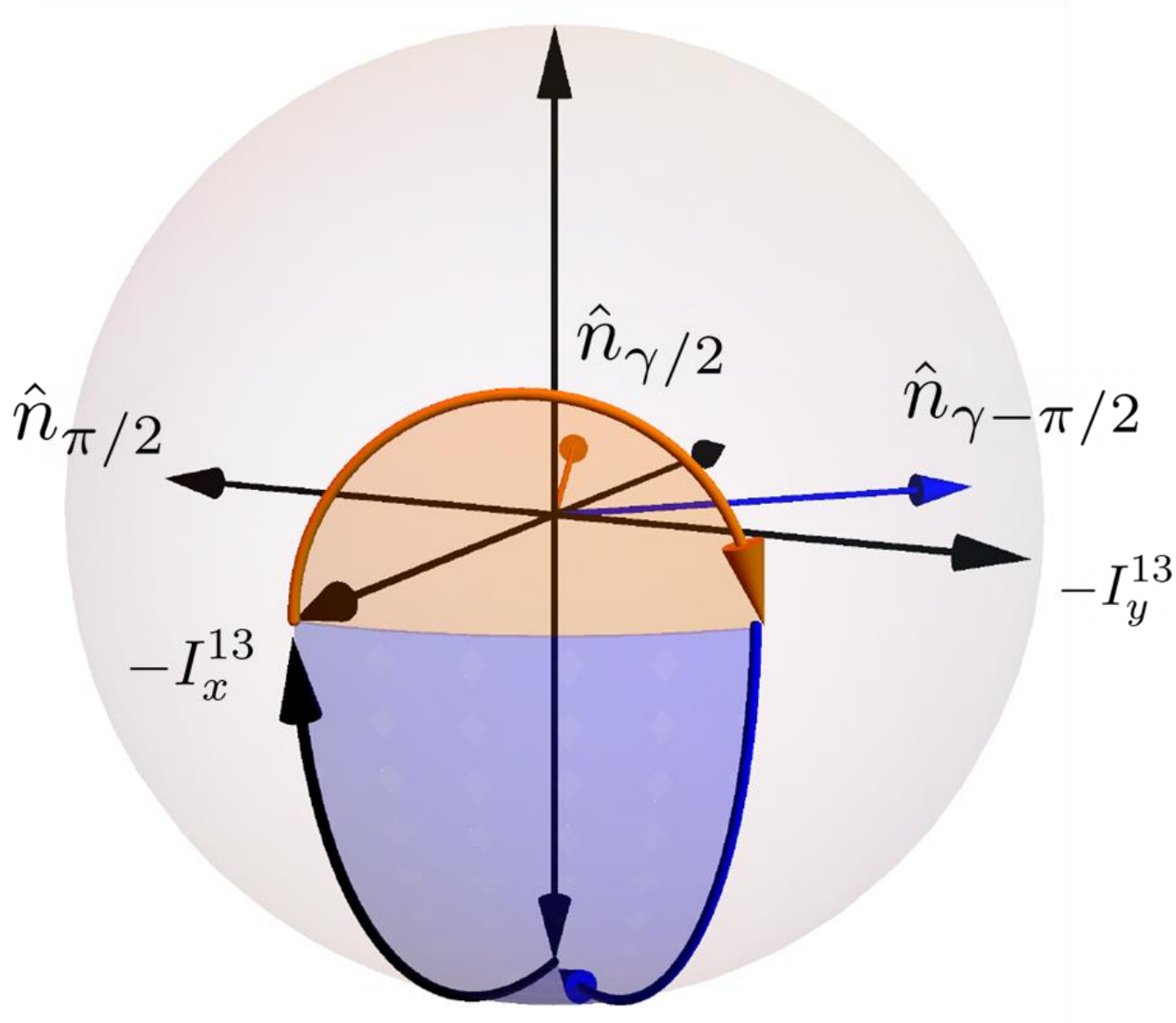

$$-I_z^{13} = |T_0\rangle\langle T_0|$$

a

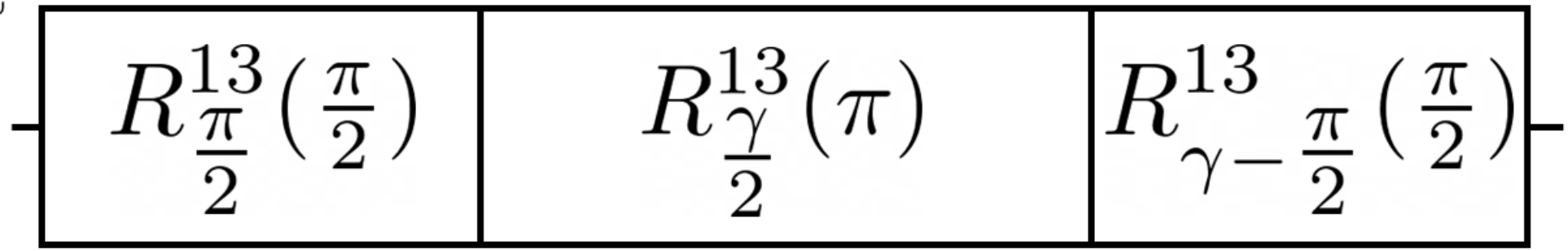

b $-\pi/2 \leq \phi \leq \pi/2$

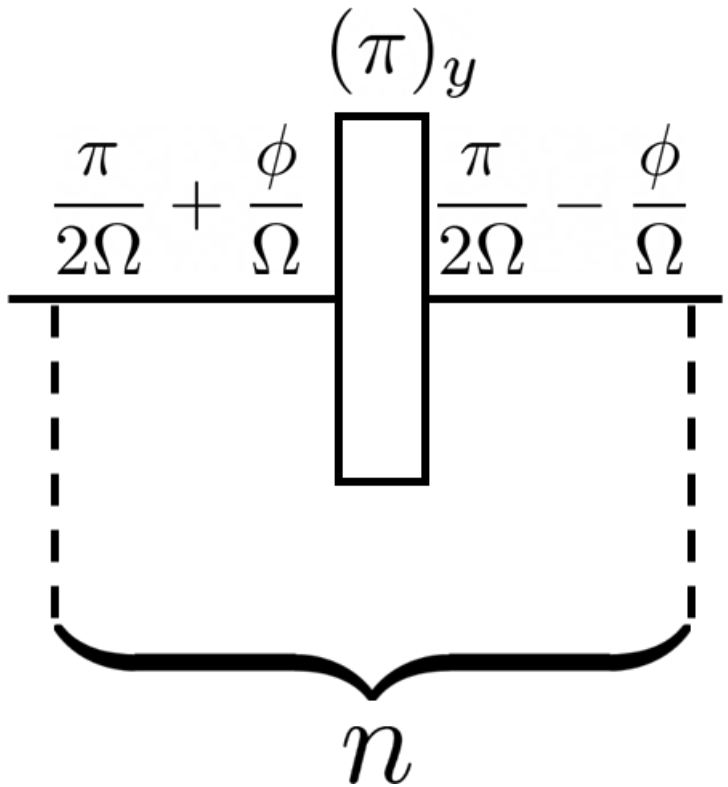

c $\pi/2 < \phi < 3\pi/2$

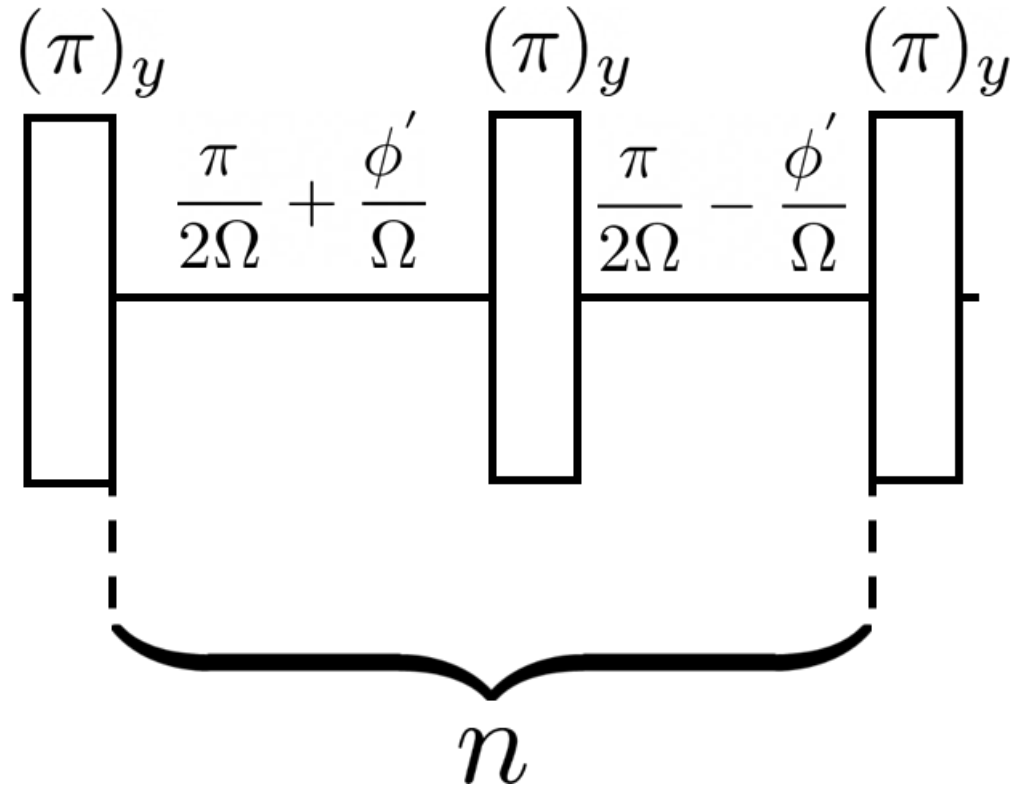

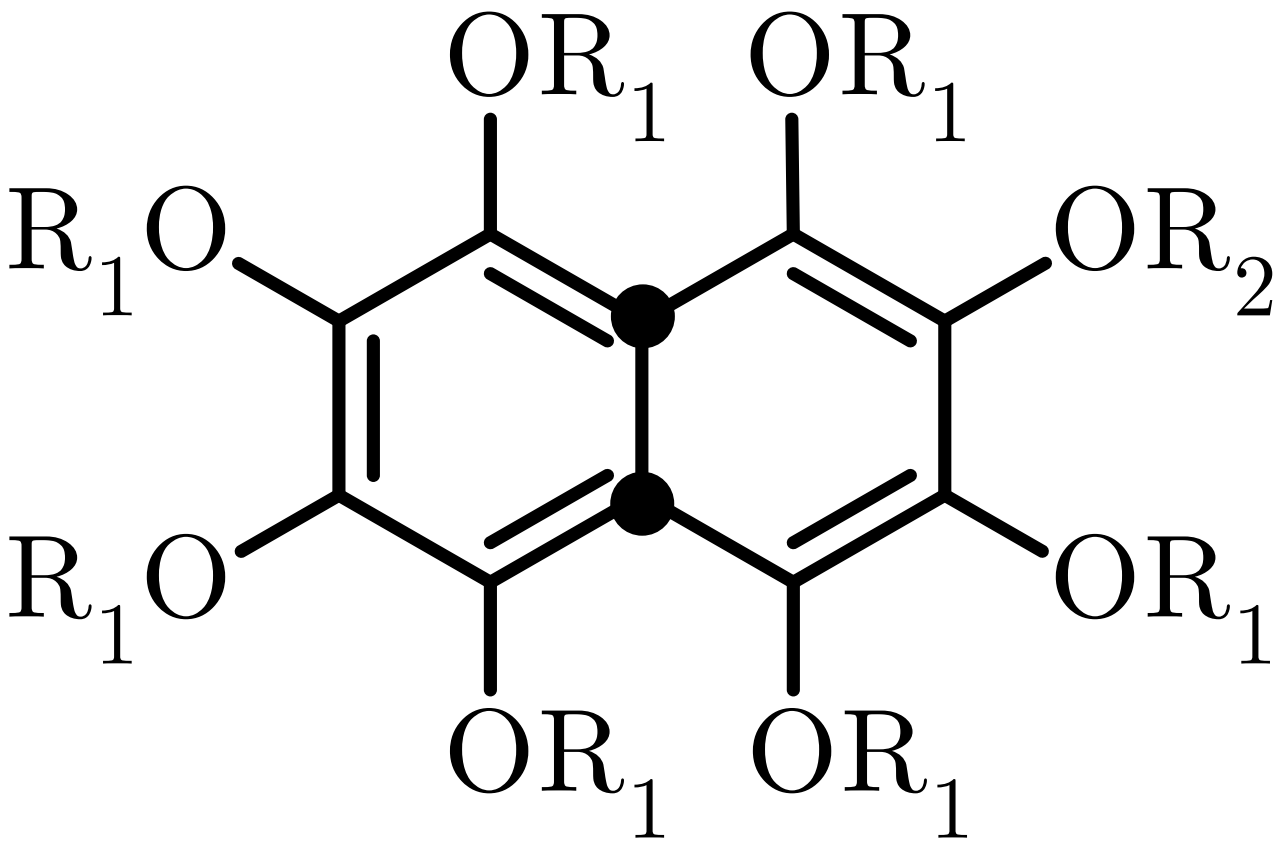

$R_1 = CD_3$

$R_2 = CD(CD_3)_2$

● = ^{13}C

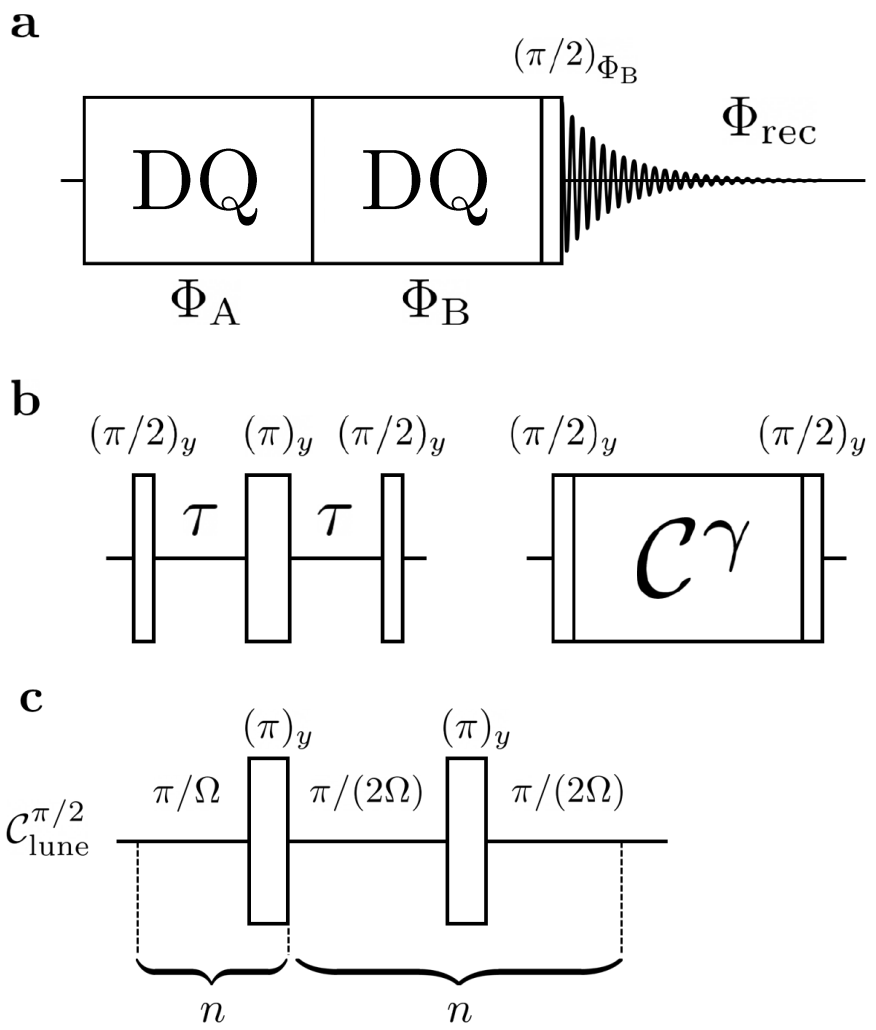
a
$(\pi/2)_{\Phi_B}$
DQ
DQ
Φ_{rec}
Φ_A
Φ_B
b
$(\pi/2)_y$
$(\pi)_y$
$(\pi/2)_y$
$(\pi/2)_y$
$(\pi/2)_y$
τ
τ
$\mathcal{C}\gamma$
c
$(\pi)_y$
$(\pi)_y$
$\mathcal{C}^{\pi/2}_{\mathrm{lune}}$
π/Ω
$\pi/(2\Omega)$
$\pi/(2\Omega)$
n
n

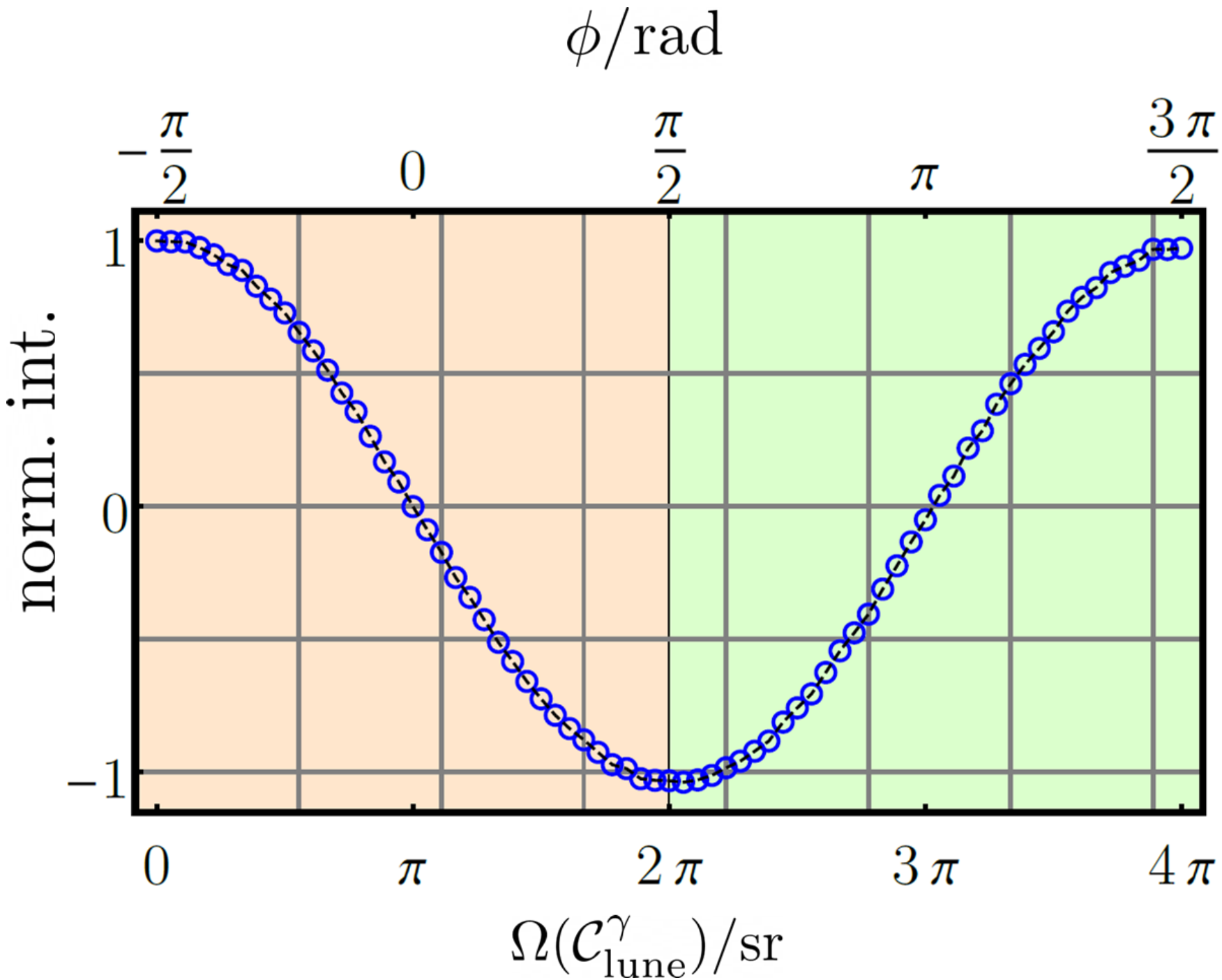
ϕ/rad
$-\frac{\pi}{2}$
0
$\frac{\pi}{2}$
π
$\frac{3\pi}{2}$
norm. int.
1
0
−1
0
π
2π
3π
4π
$\Omega(\mathcal{C}^{\gamma}_{\mathrm{lune}})$/sr

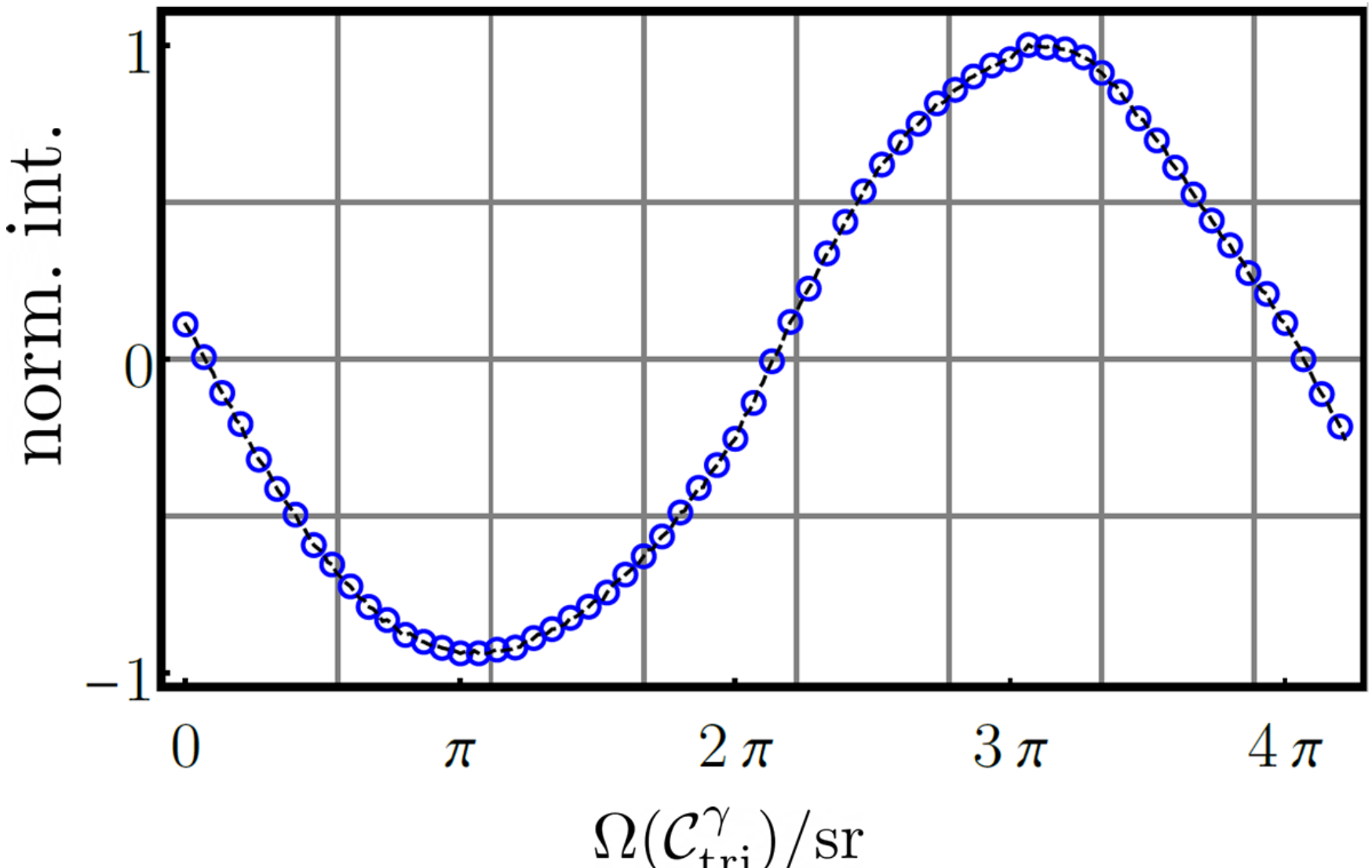
norm. int.
1
0
−1
0
π
2 π
3 π
4 π
$\Omega(\mathcal{C}^{\gamma}_{\mathrm{tri}})/\mathrm{sr}$

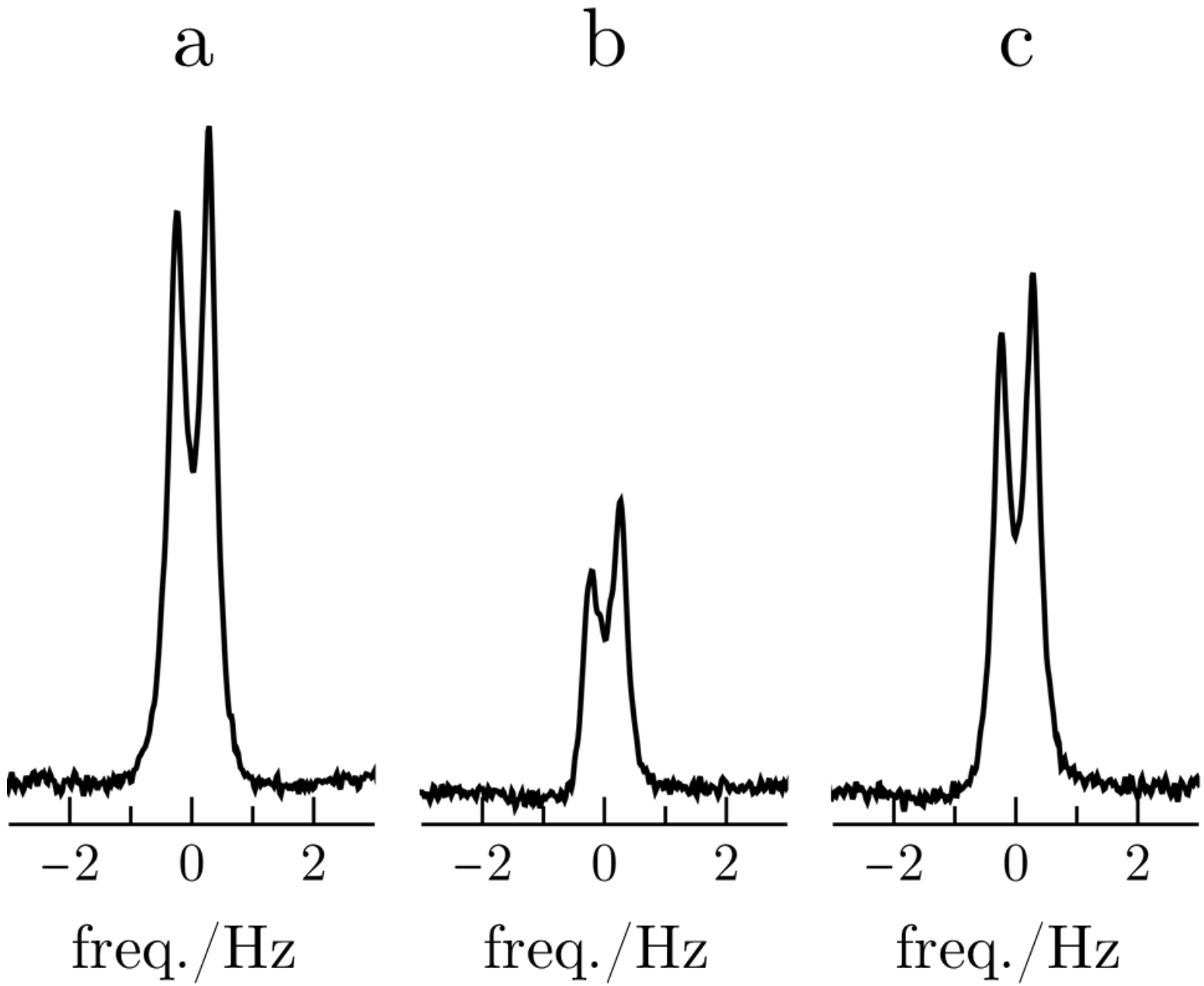
a
b
c
−2
0
2
freq./Hz
−2
0
2
freq./Hz
−2
0
2
freq./Hz